Author Summary

The myelin sheath that surrounds the axon of a neuron acts as a biological insulator. Its major function is to increase the speed at which impulses propagate along myelinated fibers in the central nervous system, as well as the peripheral nervous system. Alterations or damage affecting this structure (demyelination) result in the disruption of signals between the brain and other parts of the body. In the rat, mutations producing demyelination have been frequently identified and characterized and have contributed to a better understanding of the genetics of myelin development, physiology, and pathology. This paper reports the molecular characterization of a recessive allele responsible for the progressive disruption of myelin that was initially observed in mutant rats, previously named demyelination (*dmy*). This mutation generates an additional splicing acceptor site in an intron of the mitochondrial Mg^{2+} transporter gene (*Mrs2*), resulting in the insertion of a 83-bp genomic DNA segment into the *Mrs2* transcript and complete functional inactivation of the mutant allele. We firstly defined the biological function of MRS2 in mammals and demonstrated the crucial and unexpected role of MRS2 in myelin physiology. Our findings might be helpful in the development of new therapeutic strategies for demyelinating syndromes.

In this report we demonstrate that the causative gene (*Mrs2*) encodes a protein that is an essential component of the major electrophoretic Mg^{2+} influx system in mitochondria [6]. This gene has orthologues in other organisms, including lower eukaryotes and plants [7,8]. The protein shares many of the properties of bacterial CorA and yeast Alr1 proteins but its specific involvement in the myelination process was not known or even suspected.

Results

dmy/dmy rats exhibit a phenotype with typical demyelination

The pathology of homozygous *dmy/dmy* rats has been reported in detail previously [4]. Mutant rats exhibit no significant differences from their control littermates until 4 weeks of age. From 5 weeks on, flaccidity of the hind limbs becomes noticeable and evolves towards complete paralysis around 7–8 weeks of age. Progressive demyelination is observed in several parts of the CNS (Figure 1), namely the corpus callosum, the capsula interna, the striatum and the cerebellar peduncle, with major effects on the ventral and lateral parts of the spinal cord. Astrogliosis, which is a major feature of myelin disorder, is observed in demyelinated areas but motor neurons remain normal and there is no sign of associated inflammation in the white matter. The *dmy* mutation can then be regarded as a mutation affecting the maintenance and turnover of myelin rather than its initial production: this is typical demyelination [9].

The *dmy* syndrome is associated with a mutation in a splicing site of *Mrs2*, a gene encoding a mitochondrial Mg^{2+} channel

Out of 687 *dmy/dmy* mutant rats, collected from the 3,252 offspring of an intercross segregating for the *dmy* mutation, 23 individuals were found to carry a recombinant haplotype between the two loci that were used for the initial genetic mapping, namely; *Prl* (prolactin) and *Hh1tts* (testis-specific histone, H1t). Further investigation of these animals, using three novel informative SSLP markers, allowed us to narrow the genetic interval containing *dmy* down to 0.22 cM, between markers *D17Kur17* and *D17Got45*. Within this critical section, we found no recombination between the *dmy* locus and either *Aldh5a1* (aldhehyde dehydrogenase family 5, subfamily A1) or *Mrs2* (mitochondrial 118 RNA splicing2) loci, among $687 \times 2 = 1{,}374$ meioses. The rat genome databases revealed that *D17Kur17* and *D17Got45* were at position 46.78-Mb and 47.26-Mb, respectively, on rat Chr 17, yielding a physical size of 0.48 Mb of DNA for the interval containing the *dmy* locus. This stretch of DNA contained 6 genes (Figure 2A).

Analysis by RT-PCR of the transcription products of these 6 genes revealed that the cDNA transcribed from the *Mrs2* gene was larger in *dmy/dmy* mutants than in the controls (Figure 2B). After sequencing, we found that the larger size of the *dmy* cDNA was due to the insertion of an 83 bp intronic sequence between exons 3 and 4. Comparison of the two genomic sequences revealed a G-to-A transition, 177 bp downstream of the end of exon 3 (Figure 2C, Figure S1), generating a novel splice acceptor site, which accounted for the addition of the 83bp stretch of intronic sequence to the mutant transcript. In addition, while the *Mrs2* gene normally encodes a 434 amino-acid protein, the intronic insertion leads to a shorter protein (106 amino acids) due to the occurrence of a stop codon as a consequence of frame shifting within the novel pseudo-exon X. The new protein consisted of the first 91 amino acids of normal (wild-type) MRS2 protein followed by an additional 15 amino acids transcribed from the intronic stretch (Figure 2D) [10]. No nucleotide alteration was observed between normal and mutant haplotypes in the cDNA transcribed from the other 5 genes (*Vmp*, *Dcdc2*, *Gpld1*, *Aldh5a1*, and *KIAA0319*). These findings strongly suggested that the G-to-A mutation in intron 3 of *Mrs2* in *dmy/dmy* rats was very likely causative of the neurological phenotype.

dmy/dmy rats exhibit morphological and biochemical features characteristic of mitochondrial deficiencies

The MRS2 protein functions as a major transporter protein (Mg^{2+}, Ni^{2+} and Co^{2+}) in yeast as well as in human cells [10,11]. When this protein is functionally defective this leads to the "petite" phenotype in yeast and to cell death in human HEK 293 cells [11,12]. Because mitochondrial diseases in mammals are often accompanied by elevated lactic acid, reduced ATP, increased cytochrome oxidase (COX) activity, and the morphological alteration of mitochondria [13–15], we measured lactic acid levels and ATP contents in the CNS and performed morphological analyses of the CNS of *dmy/dmy* rats.

Lactic acid concentration in the cerebrospinal fluids was significantly elevated in *dmy/dmy* rats when compared with normal littermates: 126 ± 43.7 mg/dL vs 25 ± 9.6 mg/dL (average $\pm$ SD), $P<0.002$ (Figure 3A). The ATP concentration was markedly reduced in *dmy/dmy* rats: 265 ± 79 μM/mg vs 99 ± 46 μM/mg (average $\pm$ SD), $P<0.005$ (Figure 3B). In the affected *dmy/dmy* rats, swollen oligodendrocytes were often observed in the white matter, showing the increased COX reaction products (Figure 3C). Ultrastructurally, their cytoplasm contained many mitochondria and Golgi apparatus-like membrane structures (Figure 3D). These findings indicated that the mitochondria of *dmy/dmy* rats were functionally defective.

Rescue of *dmy/dmy* mutant phenotypes by transgenic complementation

To ascertain that the molecular defect (*i.e.* G-to-A transition) observed in the *dmy* mutant haplotype was causative of the abnormal phenotype observed in *dmy/dmy* rats, we attempted to rescue the mutant phenotype by transgenic complementation. We

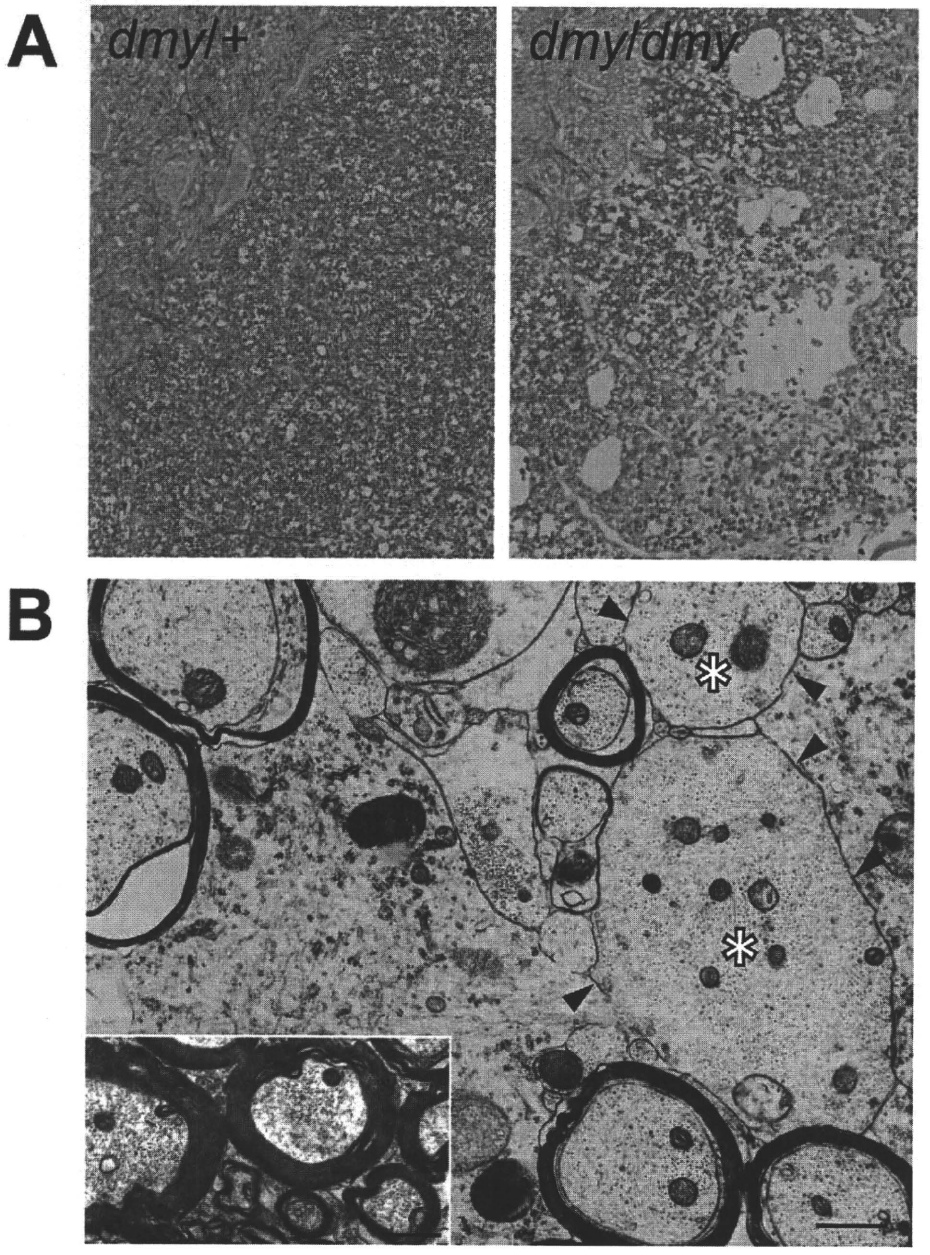

Figure 1. Demyelination in *dmy/dmy* rats. A. Histopathology of the cervical part of the spinal cord of *dmy/+* (left) and *dmy/dmy* (right) rats aged 10 weeks. Luxol fast blue-HE staining. Original magnification: ×100. B. Electron microscopy of the cervical part of spinal cord of *dmy/dmy* rats (10 weeks). Naked axons with demyelination (arrowheads) are indicated by asterisks. Inset: control image of the spinal cord from the age-matched wild type rat. Axons are normally myelinated. Bar = 1 μm.
doi:10.1371/journal.pgen.1001262.g001

established two independent WTC.DMY-*dmy* lines, expressing each *Mrs2* wild-type cDNA under the control of a cytomegalovirus (CMV) promoter (Figure S2A), and found that all *dmy/dmy* transgenic rats exhibited a completely normal phenotype, with no paralysis of the hind limbs. Histopathological analyses demonstrated that both transgenic lines no longer exhibited any sign of demyelination of the CNS (Figure S2B). In addition, lactic acid levels of the cerebrospinal fluid of transgenic *dmy/dmy* rats had returned to the normal range (Figure S2C). Electron microscopic observations revealed that mitochondria of the oligodendrocytes in transgenic rats were normal in their morphology and number (Figure S2D). These findings confirmed that the molecular changes reported above and observed in the *Mrs2* gene were indeed causative of the *dmy*-mutant phenotypes. For this reason we decided that the symbol of the mutant allele should, from now on, be changed to $Mrs2^{dmy}$.

MRS2-GFP recombinant protein is expressed in the mitochondria

To characterize the tissues and cell types expressing MRS2 as well as the subcellular localization of this protein in the CNS, we generated a strain of rats transgenic for a recombinant MRS2-GFP BAC clone. These transgenic rats were expected to express recombinant protein under the control of the endogenous, normal *Mrs2* promoter. We found that cytoplasmic dot-like MRS2-GFP

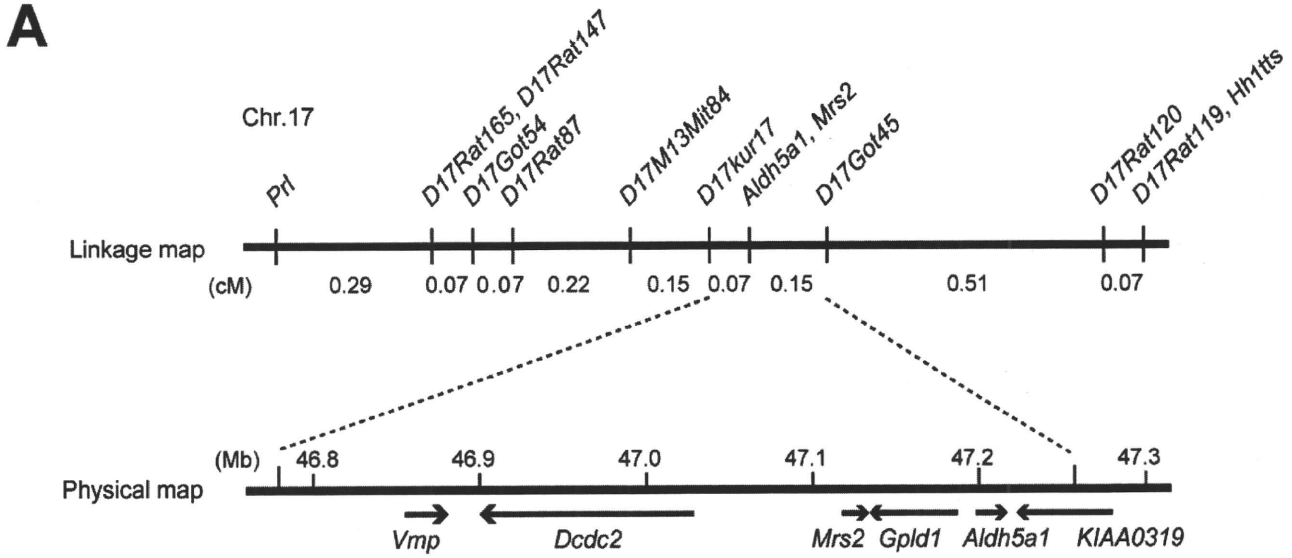
A
Chr.17
Prl
D17Rat165, D17Rat147
D17Got54
D17Rat87
D17M13Mit84
D17kur17
Aldh5a1, Mrs2
D17Got45
D17Rat120
D17Rat119, Hh1tts
Linkage map
(cM)
0.29
0.07 0.07
0.22
0.15 0.07 0.15
0.51
0.07
(Mb)
46.8
46.9
47.0
47.1
47.2
47.3
Physical map
Vmp
Dcdc2
Mrs2 Gpld1 Aldh5a1 KIAA0319

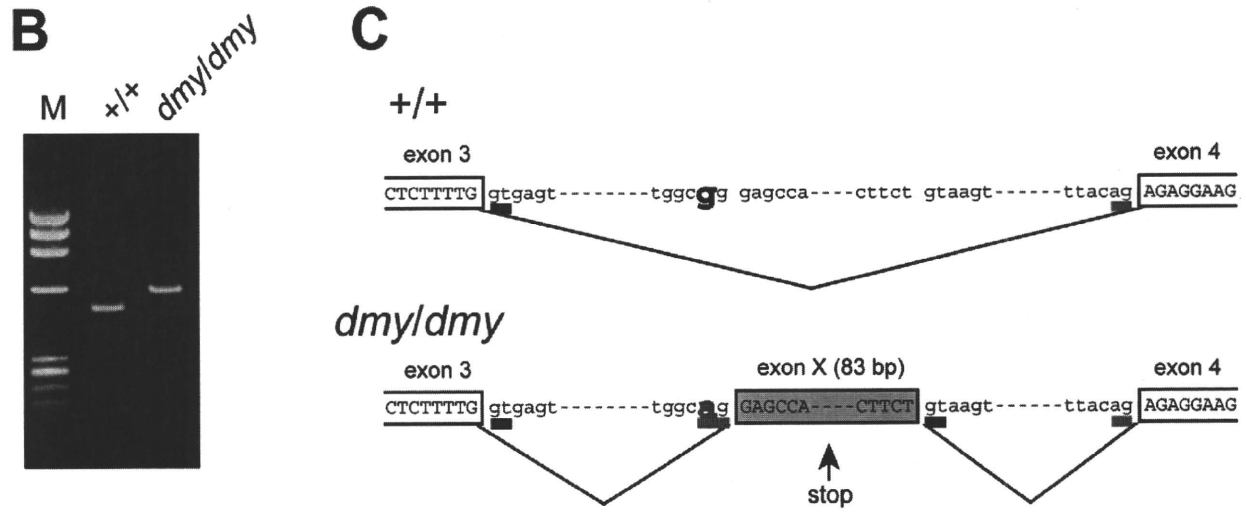
B
M
+/+
dmy/dmy
C
+/+
exon 3
exon 4
CTCTTTTG gtgagt--------tggcgg gagcca----cttct gtaagt------ttacag AGAGGAAG
dmy/dmy
exon 3
exon X (83 bp)
exon 4
CTCTTTTG gtgagt--------tggcag GAGCCA----CTTCT gtaagt------ttacag AGAGGAAG
stop

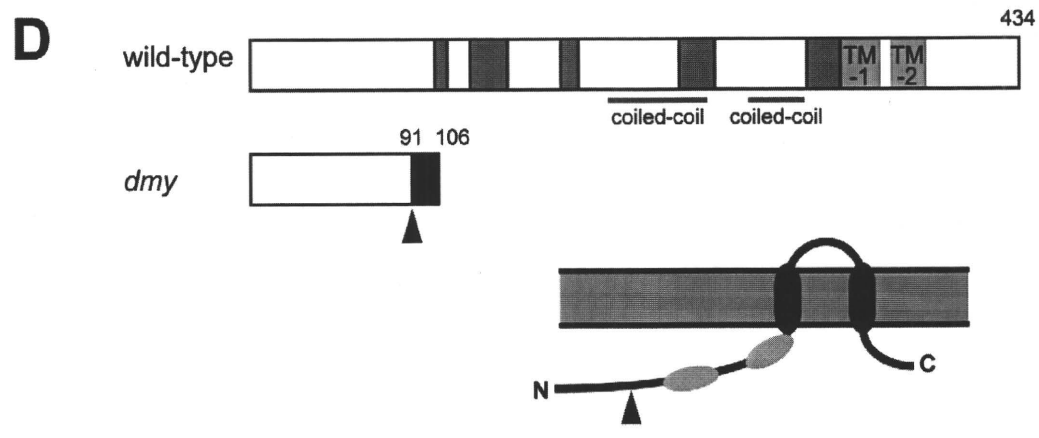
D
wild-type
434
TM -1
TM -2
coiled-coil
coiled-coil
91 106
dmy
N
C

Figure 2. Positional cloning of the *dmy* mutation. A. The *dmy* locus was localized within a 0.22-cM region of chromosome 17 between *D17Kur17* and *D17Got45* and no recombination was observed with SSLP markers designed from *Aldh5a1* and *Mrs2* genomic sequences in 1,374 informative meioses. Within the 0.48-Mb physical interval between *D17Kur17* and *D17Got45*, harboring the *dmy* locus, 6 genes: *Vmp* (vesicular membrane protein p24), *Dcdc2* (doublecortin domain containing 2), *Mrs2* (MRS2 magnesium homeostasis factor (*S. cerevisiae*), *Gpld1* (glycosylphosphatidylinositol specific phospholipase D1), *Aldh5a1* (aldehyde dehydrogenase family 5, subfamily A1), and *KIAA0319*, were previously mapped. B. A larger RT-PCR product was obtained when amplifying the 5′ region of *Mrs2* cDNAs from *dmy/dmy* rats with a primer set of rMrs2l-3&4 (5′-TGTACTGATCTACCCGAGTTCC-3′ and 5′-TCTGGAGTTATCACAGCCTTCA-3′). M: molecular marker, ΦX174-*Hae*III digest. C. Upper: Genomic organization in the vicinity of intron 3 of the *Mrs2* wild-type allele. Lower: Genomic rearrangements in the same intron 3 of the $Mrs2^{dmy}$ mutant allele. In the $Mrs2^{dmy}$ mutant allele, a novel splice acceptor site was generated as a consequence of a G-to-A transition at 177 bp downstream of the end of exon 3. An 83-bp genomic sequence (boxed in gray), downstream of the recently generated acceptor site (tggcag), is then inserted into the *Mrs2* mutant transcript. This sequence contains a premature stop codon (vertical arrow), which truncates the protein almost immediately downstream of exon 3. D. Schematic representations of the wild-type and *dmy* MRS2 proteins. Conserved amino acid residues and transmembrane domains are indicated by grey and purple boxes, respectively. Coiled-coil regions are indicated by horizontal orange lines. The position of the *dmy* mutation is indicated by an arrowhead, and the additional 15 residues (GATWTPRILEECLES), indicated by a black box, are deduced to be added subsequently. Bottom: Schematic representation of the topology of MRS2. Purple: transmembrane domains, Orange: coiled-coil regions. The position of the *dmy* mutation is indicated by an arrowhead.
doi:10.1371/journal.pgen.1001262.g002

signals were observed in neurons throughout the CNS. To a lesser extent, astrocytes and oligodendrocytes also exhibited occasional expression of MRS2 (Figure S3). Confocal microscopy demonstrated that MRS2 is located in the mitochondria (Figure 4A–4C). Moreover, immunoelectron microsopic examinations with anti-GFP antibody revealed that MRS2 is localized in the inner membrane of the mitochondria (Figure 4D). MRS2 expression was also observed in the myocardium, liver, testis and skeletal muscles (Figure S4).

Microglia activation and high expression of inflammatory cytokines were observed in $Mrs2^{dmy}/Mrs2^{dmy}$ rats

Microglial activation, characterized by cellular hypertrophy, has been reported in various dysmyelinating and demyelinating pathologies. To assess microglial activation, we performed immunohistochemistry for IBA1, a specific marker of microglia. In $Mrs2^{dmy}/Mrs2^{dmy}$ rats, prolonged activation of microglia was prominently observed at 6–7 weeks of age (Figure 5A and 5B), the stage at which clinical symptoms such as flaccid paralysis were commonly observed. Expression levels of proinflammatory cytokines, such as *Il1b* and *Il6*, were also significantly higher in $Mrs2^{dmy}/Mrs2^{dmy}$ rats than in wild-type littermates at 6 weeks of age (Figure 5C).

Discussion

Characterization, by positional cloning, of the molecular defect responsible for the demyelinating phenotype observed in adult *dmy/dmy* rats led us to incriminate a mutation in the *Mrs2* gene. No mutant allele before $Mrs2^{dmy}$, which we report here, has ever been reported at this locus in any mammalian species.

Mrs2 encodes an inner membrane Mg^{2+} channel in mitochondria and belongs to a family with orthologous copies in a wide range of species [10,12]. *Mrs2* was originally identified in yeast, and orthologous copies of this gene have been identified in a variety of organisms, including bacteria (CorA), fungi (Alr1), and plants (AtMrs2). All proteins in the family have the same substrate selectivity: they transport Mg^{2+}, Co^{2+} and some other divalent cations across the mitochondrial membrane. Even if these proteins exhibit relatively low sequence similarities, they all have a few important domains at the same relative position and can functionally complement each other over a wide range of phylogenetic distances [16,17]. In mammals, the normal protein MRS2 has two universally conserved transmembrane domains (TMs) and a conserved Gly-Met-Asn (GMN) motif close to the first TM domain that forms part of the pore and is essential for Mg^{2+} transport [18] (Figure 2D, Figure S5). As we demonstrated, the protein is truncated in *dmy/dmy* mutant rats, having lost both of its essential domains and accordingly its function of an Mg^{2+} transmembrane transporter. In other words, $Mrs2^{dmy}$ is a null allele, which is totally consistent with its recessive allelic interaction.

An MRS2 is a major transport for Mg^{2+} uptake into mitochondria, its function would be expected to be important, if not essential, for the maintenance of respiratory complex I and accordingly for cell viability [6,11]. This assumption was supported by the analysis of MRS2 knock-down, mediated by shRNA in a human HEK-293 cell line, which resulted in a series of physiological changes ranging from transient reduction of Mg^{2+} uptake to the complete loss of mitochondrial respiratory complex I, with decreased mitochondrial membrane potential and cell death, depending on the duration of knock-down treatment [11]. However, if we consider the phenotype of our mutant rat, which is apparently limited to the myelination process with a rather long lifespan, the role of MRS2 in the maintenance of cell integrity should be reconsidered.

Considering the pathological features that appear to be characteristics of the $Mrs2^{dmy}$ allele on the one hand, and MRS2-specific functions, as described above on the other, it is logical to consider that the demyelinating syndrome in mutant rats results from a mitochondrial disease. This assertion is supported by the observation of an elevated rate of lactic acid in the cerebrospinal fluid, reduced ATP in the brain, increased COX activity, and the morphological alteration of mitochondria, which is generally considered a major characteristic of mitochondrial diseases [13–15]. An increase in mitochondria is characteristic of cells with reduced respiratory capacity [19]. The association of mitochondrial dysfunction with demyelination (or leukodystrophy) has been already reported in Leigh syndrome and mitochondrial DNA depletion syndrome [20–23]. The tissues most frequently affected in these mitochondrial diseases are the cerebrum, peripheral nerves, and skeletal muscles, presumably because cells of these tissues require more energy than any other cells in the body. Unfortunately, the detailed pathophysiological mechanism(s) leading to demyelination in these diseases has not yet been unraveled. We consider that our mutant rat could be an interesting tool for investigating this matter.

Mitochondrial dysfunction has also been observed in multiple sclerosis (MS), one of the most common demyelination diseases, but here again many aspects of the pathophysiology require further investigation [24,25]. This difficulty of linking gene functions with a specific syndrome is not so surprising if we consider that, according to the most recent estimates, there may be as many as 1,500 nuclear-encoded mitochondrial proteins [26] and that less than half have been identified with experimental support. Clearly, a complete protein inventory of this organelle

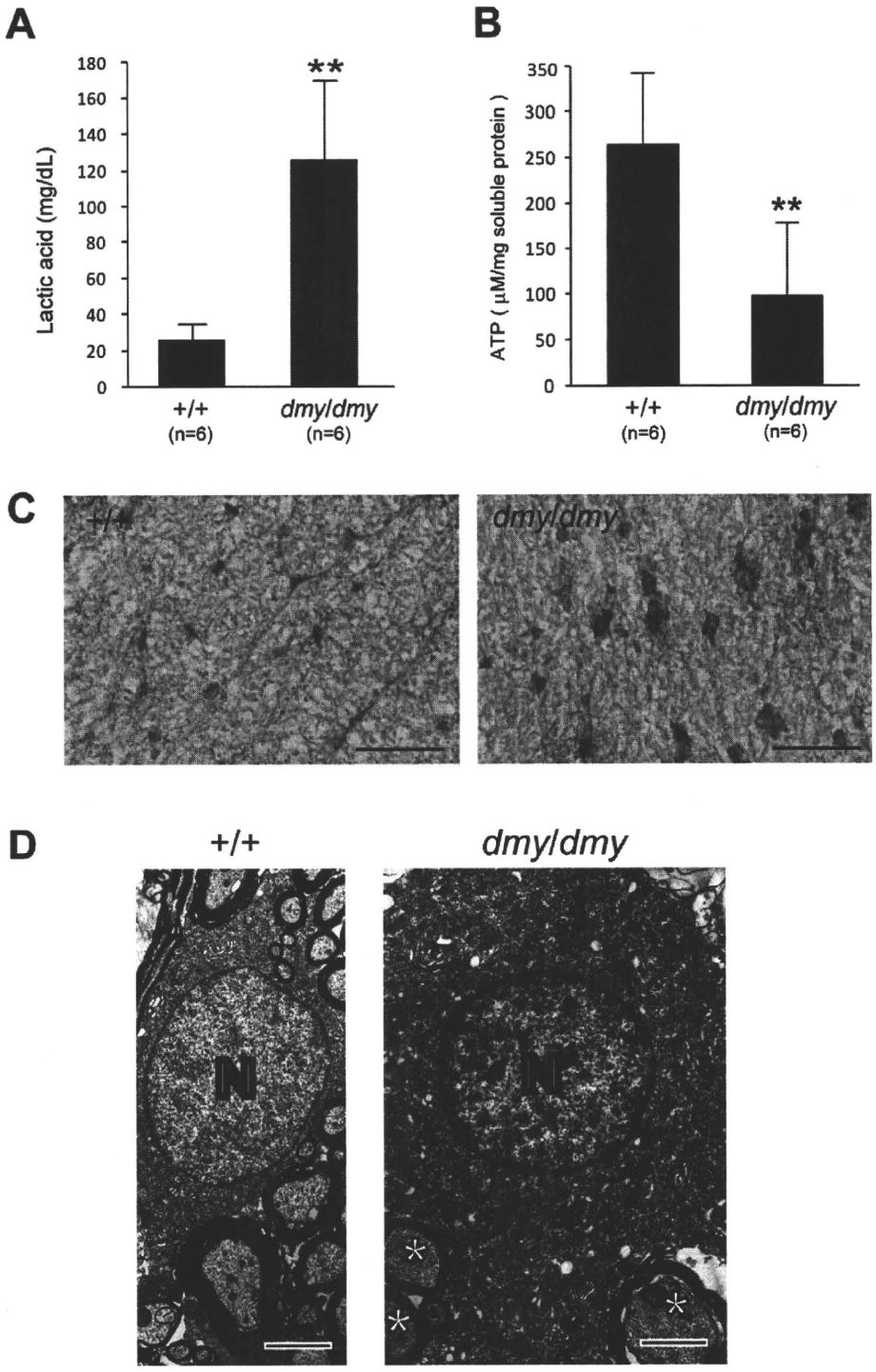

Figure 3. Biochemical and morphological abnormalities in the mitochondria of *dmy/dmy* mutant rats. A. Lactic acid concentration in cerebrospinal fluid of 6–7-week-old *dmy/dmy* rats and age-matched wild-type rats. **, $P<0.002$. B. ATP levels in the brain of 6–7-week-old *dmy/dmy* rats and age-matched wild-type rats. **, $P<0.005$. C. Cytochrome oxidase staining of the spinal cords of 6–7-week-old *dmy/dmy* (right) and age-matched wild-type (left) rats. Swollen oligodendrocytes were often seen they showed increased COX reaction product. Bar = 50 μm. D. Electron microphotographs of a swollen oligodendrocyte in a *dmy/dmy* rat (right) and an oligodendrocyte in a control wild-type rat. White matter of thoracic spine at 6 weeks of age. N: Nucleus of the oligodendrocyte. Axons adjacent to the oligodendrocyte are indicated by asterisks. Bar = 2 μm.
doi:10.1371/journal.pgen.1001262.g003

across tissues would provide a molecular framework to relate mitochondrial biology and pathogenesis [27].

A point concerning *Mrs2* gene expression in the CNS that is worth noting after our experiments and observations is that the gene in question is expressed at a higher rate in neurons than in oligodendrocytes (Figure 4, Figure S3). This was rather unexpected if we consider that oligodendrocytes are the cells actually responsible for myelination of the CNS. At this time, it remains

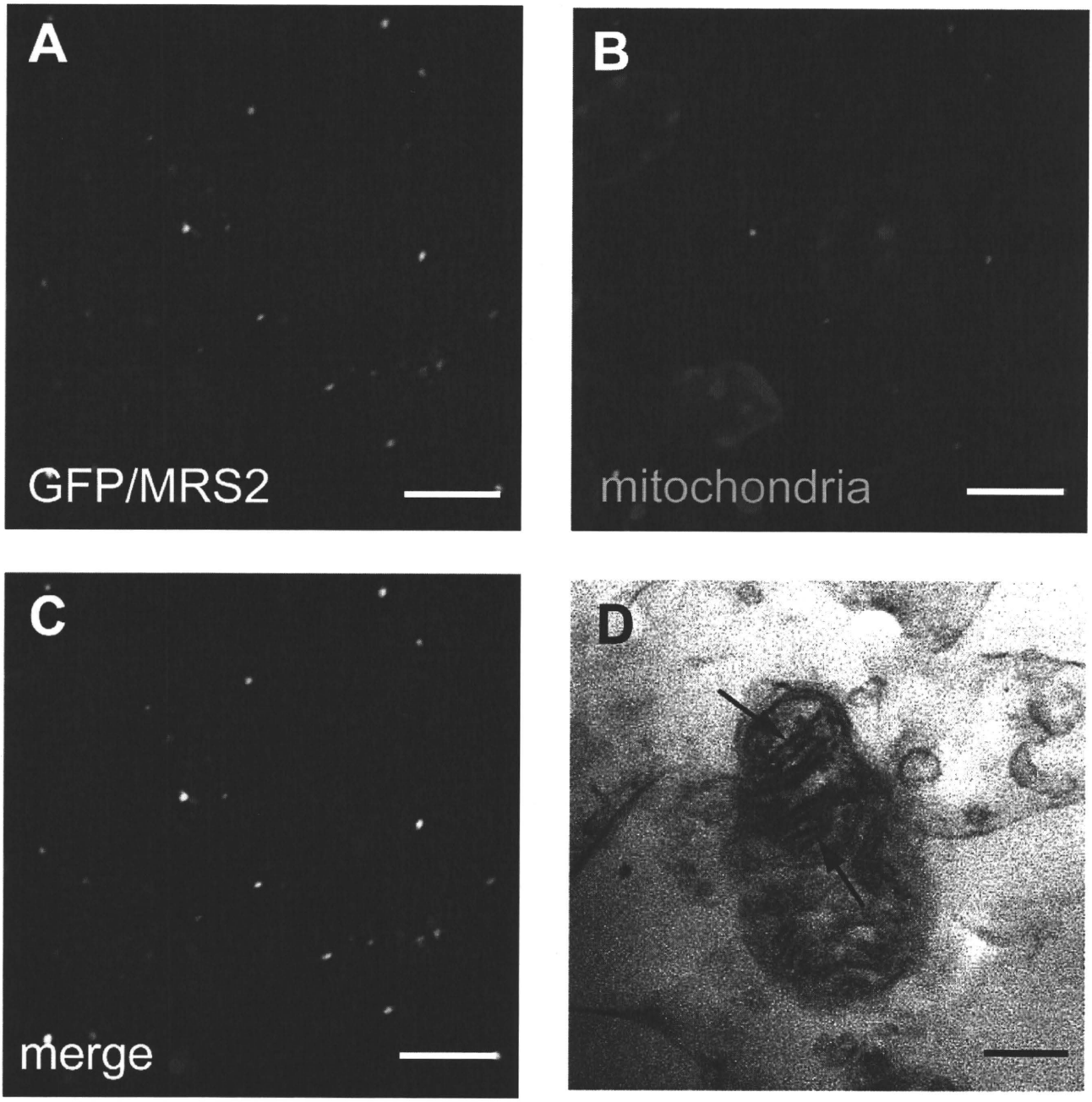

Figure 4. Expression of MRS2 protein in the mitochondria. MRS2-GFP recombinant protein (Green) was seen in the cytoplasm of pyramidal cells (A). MRS2-GFP signals were colocalized with the mitochondria (B), as shown in the confocal image of GFP and mitochondrial immunohistochemistry (C). Nuclei were stained with DAPI (Blue). Bar: 5 μm. Immunoelectron microscopy using anti-GFP antibody revealed that MRS2-GFP signals were localized in the inner membrane of the mitochondria (arrows) (D). Bar: 200 nm.
doi:10.1371/journal.pgen.1001262.g004

unclear whether the demyelination in *dmy/dmy* rats is triggered cell-autonomously or cell-nonautonomously. Instead, it is likely that demyelination is enhanced by the surrounding cells, such as activated microglia and astroglia. At 6 weeks of age, when *dmy/dmy* rats began to exhibit ataxia [9], cytokine levels were elevated and microglia were activated (Figure 5), and it is considered that activated microglia cause neuronal damage through the release of potentially cytotoxic molecules, such as proinflammatory cytokines, reactive oxygen intermediates, proteinases, and complement proteins [28]. Oligodendrocytes show greater vulnerability to such molecules [29,30]. Additionally, Kuwamura and co-workers reported prominent astrogliosis and many ED-1-positive macrophages in myelin-destroyed areas [9]. When considered together, these morphological observations led us to believe that the demyelination observed in *dmy/dmy* rats is probably enhanced by activated microglia and astroglia.

In summary, we identified $Mrs2^{dmy}$ as a loss-of-function mutation of the *Mrs2* gene that normally encodes Mg^{2+} transporter protein of the mitochondrial inner membrane. Our observations also demonstrate that the mechanisms underlying the

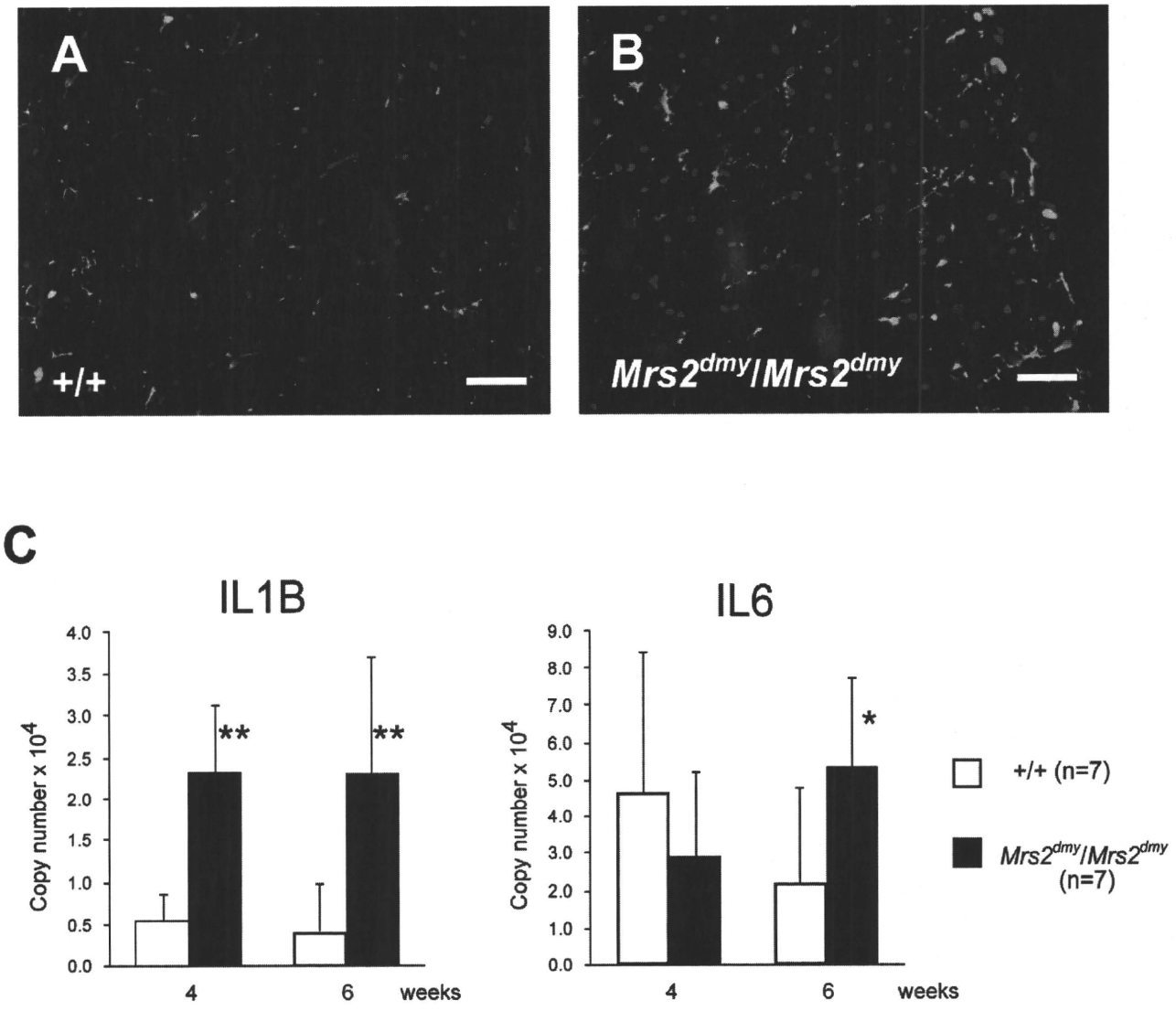

Figure 5. Activation of microglia in the central nervous system of *Mrs2*^{dmy}/*Mrs2*^{dmy} rats. Immunohistochemistry for Iba1 in the lumbar part of the spinal cord of wild-type (A) and *Mrs2*^{dmy}/*Mrs2*^{dmy} rats (B) at 6 weeks of age. Signals of Iba1 (AlexaFluor 546 nm; red), which is upregulated during the activation of microglia, are seen in *Mrs2*^{dmy}/*Mrs2*^{dmy} rats much more the wild-type control. Nucleus is stained with DAPI (blue). C, Inflammatory cytokine mRNA expression in the CNS of wild-type (□) and *Mrs2*^{dmy}/*Mrs2*^{dmy} (■) rats. IL1b expression was elevated in *Mrs2*^{dmy}/*Mrs2*^{dmy} rats at 4 and 6 weeks of age. IL6 was elevated in *Mrs2*^{dmy}/*Mrs2*^{dmy} rats at 6 weeks of age. * $P<0.05$, ** $P<0.005$.
doi:10.1371/journal.pgen.1001262.g005

initial development of myelin (myelination) are different from those that are involved in its maintenance and turnover since, in *Mrs2*^{dmy}/*Mrs2*^{dmy} rats, myelin development is normal while its maintenance is defective. Our mutant rats also appear to be an excellent animal model, not only to evaluate the causal relationships between primary mitochondrial dysfunction and subsequent demyelination, but also for the development of therapies making use, for example, of cell transplantation.

Materials and Methods

Genetic fine mapping of *dmy*

Congenic strains WTC (NBRP#0020) and WTC.DMY-*dmy* (NBRP#0021) were both from the National BioResource Project - Rat, Kyoto University (Kyoto, Japan). (WTC.DMY-*dmy* × BN/SsNSlc)F1(+/*dmy*) rats were intercrossed to produce F2 progeny. *dmy*/*dmy* homozygotes were identified at 7–8 weeks of age, when paralysis of the hind limbs was obvious. 687 *dmy*/*dmy* rats were collected out of 3,252 F2 animals (~21%) and used for fine mapping of the *dmy* locus. Simple sequence length polymorphisms (SSLPs) from the *Prl* (prolactin) and *Hh1tts* (Testis-specific histone, H1t and H4t) genes were used for genotyping as described [31]. To refine the limits of the recombinant interval between *Prl* and *Hh1tts*, two gene-specific and one anonymous SSLP markers were used: *Mrs2* (5′-TCTCCCTTGCCTCTATCTCTCGTCT-3′,5′-CCTGCAGTACTGGGTAAGCCTGATG-3′), *Aldh5a1* (5′-GTTAACTGCACAAGAGCAAGCCAGT-3′, 5′-GCTAATGTTAAGTCATGGGGTGAGG-3′), and *D17Kur17* 5′-ACCTCTTTTTGCCAGCATTG-3′, 5′-CCCTGGGATTGGTCCATA-3′).

All animal experiments were approved by the Animal Research Committee of Kyoto University and were conducted according to the Regulations on Animal Experimentation of Kyoto University.

RT-PCR and direct sequencing

Total RNA was isolated from the brain of 5-week-old animals using ISOGEN (NIPPON GENE, Tokyo, Japan). RT-PCR and direct sequencing of the PCR products were carried out as described previously [32].

Transgenic rescue and recombinant BAC transgenics

A construct containing the CMV promoter, 1.45-kb of the *Mrs2* coding sequence, and SV40 polyA signal was excised from the vector (pCMV-Script; Agilent Technologies, CA, USA) and used as a transgene, which was microinjected into the pronuclei of fertilized oocytes collected from Crj:Wistar rats. Transgenic offspring founder rats were then crossed with WTC- +/*dmy* rats and then backcrossed again to WTC- +/*dmy* rats to obtain *dmy/dmy* homozygous and also hemizygous for the transgene (*dmy/dmy*, tg/-). Expression of the transgene was confirmed by RT-PCR with primers (5′-GCGAATGGAGATCCAATTTT-3′, 5′-GGGAGGTGTGGGAGGTTTT-3′) to detect SV40 polyA sequence. Brain RNA was treated with DNase I (New England BioLabs) to remove contaminating genomic DNA and then subjected to cDNA synthesis.

A rat BAC clone, CHORI-230-9K13, including the rat *Mrs2* gene was modified to express MR2SL-EGFP fusion protein under the endogenous promoter by ET recombination technology [33]. Modified genomic DNA was excised from the vector and then used for *in ovo* transgenesis.

Quantitative PCR

Real-time PCR was performed using the Thermal Cycler Dice Real Time System (Takara Bio Inc., Otsu, Japan) with SYBR Premix Ex Taq II (Takara Bio Inc., Otsu, Japan). By monitoring amplification curves of a test sample and reference samples that contained 101–106 molecules of the gene of interest, the number of target molecules in the test sample was analyzed. The number of target molecules was normalized to that of glyceraldehyde-3-phosphate dehydrogenase (*Gapdh*) as an internal control. The primers used are as follows: 5′-GCTGTGGCAGCTACCTATGTCTTG-3′ and 5′-AGGTCGTCATCATCCCACGAG-3′ for the rat Interleukin-1b (*Il1b*), 5′-CCACTTCACAAGTCGGAGGCTTA-3′ and 5′-GTGCATCATCGCTGTTCATACAATC-3′ for the rat interleukin-6 (*Il6*), 5′-GGCACAGTCAAGGCTGAGAATG-3′ and 5′-ATGGTGGTGAAGACGCCAGTA-3′ for rat *Gapdh*.

Electron microscopy

Perfusion fixation through the left ventricle was conducted with 4% paraformaldehyde in 0.1 M phosphate buffer (PB). Brains and spinal cords were dissected and stored in 2% paraformaldehyde and 2.5% glutaraldehyde in 0.1 M PB, then post-fixed with 2% osmic acid for 2 hours and embedded in epoxy resin. Ultrathin sections were double-stained with uranyl acetate and lead citrate and examined by a Hitachi H-7500 electron microscope (Hitachi, Tokyo, Japan).

Immunohistochemistry

Immunohistochemistry was performed as described previously [9]. The following primary antibodies were used: monoclonal anti-2′, 3′-cyclic nucleotide-3′-phosphodiesterase (CNPase) for oligodendrocytes (1:1,000; Sigma, St. Louis, MO, USA), monoclonal anti-mitochondria (1:100; Abcam, Cambridge, MA, USA), polyclonal anti-GFAP for astrocytes (1:1,000; Dako, Carpinteria, CA, USA), polyclonal anti-Iba1 for microglia/macrophages (1:200; Wako Pure Chemical Industries, Osaka, Japan). Cy3-conjugated anti-mouse IgG (1:500; Jackson Laboratories) or Alexa 588-conjugated anti-rabbit IgG (1:500; Molecular Probes) antibody was reacted. Nuclei were counterstained with DAPI (Vactor Laboratories). Signals were detected with a fluorescence microscopy (Olympus, Tokyo, Japan) or a confocal imaging system (C1Si; Nikon, Tokyo, Japan).

For immunoelectron microscopy, PFA-perfused frozen sections were incubated with rabbit antibody against fluorescent protein (1:2,000; Molecular Probes) at 4 °C overnight. After washing in PBS, peroxidase-conjugated anti-rabbit IgG Fab fraction (Jackson Laboratories, 1:1,000) and immunoreactions were reacted 3,3-diaminobenzidine substrate kit (Vector Laboratories), postfixed in 1% osmium tetraoxide, dehydrated in graded ethanol, and then embedded in epoxy resin. Ultrathin sections were examined by electron microscopy (Hitachi, Tokyo, Japan).

Lactic acid measurements

Cerebrospinal fluid was collected from *dmy/dmy*, wild-type littermates, and *dmy/dmy* with the normal *Mrs2* transgene at 6–7 weeks of age under isoflurane anesthesia. They were then mixed with 0.8N perchloric acid to inactivate proteins. After centrifugation, lactic acid concentrations of the supernatants were measured by Determiner LA (KYOWA MEDEX Co., Ltd., Tokyo, Japan).

Cytochrome oxidase histochemistry

Frozen spinal cord sections were prepared. Then, 100 µl of freshly prepared reaction buffer [50 mM Tris/HCl (pH 7.4), 0.5 mg/ml diaminobenzidine, 20 µg/ml catalase and 0.50 mg/ml cytochrome C] was added to each section and slides were incubated for 30 min at 37°C.

ATP measurements

Rats were sacrificed by cervical dislocation and the brains were immediately excised, frozen in liquid nitrogen, and stored at −80°C until measurement. In order to release cellular ATP, frozen tissue (25 mg) was boiled for 2 min after the addition of 300 µl water containing 100 mM Tris/HCl (pH 7.75) and 4 mM EDTA. Samples were placed on ice and homogenized by sonification (micro tip, 1 s ×10 pulse). ATP concentrations were determined using the ATP bioluminescence assay kit HS II (Roche) according to the manufacturer's protocol. Data were standardized to the protein concentration which was determined by Coomassie Plus – the better Bradford assay kit (Pierce).

Statistical analysis

Statistical differences in lactic acid, ATP and mRNA expressions between wild-type and *dmy/dmy* rats were evaluated using the Mann-Whitney U test.

Supporting Information

Figure S1 Detection of the $Mrs2^{dmy}$ mutation. A. Chromatograms showing the $Mrs2^{dmy}$ G-to-A mutation. Upper: wild-type genome. Lower: $Mrs2^{dmy}/Mrs2^{dmy}$ genome. The $Mrs2^{dmy}$ mutation disrupted *Aci*I restriction site (GGCG) in the $Mrs2^{dmy}/Mrs2^{dmy}$ genome. B. Molecular diagnosis of the $Mrs2^{dmy}$ mutation. In the wild type, the 349-bp PCR product amplified with primers rMrs2-31&32 (5′-AAAGTTTGACAAAGAAGGAAACG-3′ and 5′-GGGGATGGAGGGCTATGTAA-3′) is digested with *Aci*I but not in $Mrs2^{dmy}/Mrs2^{dmy}$ mutant rats. M: ΦX174-*Hae*III digests.
Found at: doi:10.1371/journal.pgen.1001262.s001 (1.15 MB TIF)

Figure S2 Transgenic rescue experiment. A. Expression of the transgene in the brain of a transgenic rat. Brain cDNA from Tg-

positive rats (Lanes 2 and 3) and Tg-negetive rats (Lanes 1and 4) was used as templates. Brain RNA was treated with DNaseI to remove contaminating genomic DNA. M: ΦX174 *Hae*III digests. B. Histopathology of the cervical part of the spinal cord of *dmy/dmy* transgene-negative rats (left) and *dmy/dmy* transgene-positive (right) rats aged 10 weeks. Luxol fast blue-HE staining. Original magnification: ×100. C. Lactic acid concentration in cerebrospinal fluid of 6-7-week-old *dmy/dmy* rats and age-matched *dmy/dmy Mrs2* cDNA-transgenic rats. Elevated lactic acid (126 ± 43.7 mg/dL) was reduced to normal level (22 ± 3.1 mg/dL). **, $P < 0.002$. D. Electron microphotograph of an oligodendrocyte in a *dmy/dmy* transgene-positive rat. Densely packed mitochondria (arrowheads) were found in the cytoplasm. Bar: 2μm.
Found at: doi:10.1371/journal.pgen.1001262.s002 (5.52 MB TIF)

Figure S3 MRS2 expression in the CNS of Mrs2-GFP recombinant BAC transgenic rats. MRS2 signals were mainly found in neurons (A), and occasionally in GFAP-positive astrocytes (B) and CNP-positive oligodendrocytes (C). Left: Bar: 50 μm. Center, Right: Bar: 20 μm.
Found at: doi:10.1371/journal.pgen.1001262.s003 (3.15 MB TIF)

Figure S4 MRS2 expression in Mrs2-GFP recombinant BAC transgenic rats. MRS2 signals were observed in the myocardium (A), liver (B), testis (C) and skeletal muscles (D). Bar: 50 μm.
Found at: doi:10.1371/journal.pgen.1001262.s004 (6.29 MB TIF)

Figure S5 Sequence alignment of yeast, human, and rat MRS2 proteins. Predicted transmembrane domains (TM-1, TM-2) are boxed; * indicates identical residues; : indicates conservative substitution; . indicates semiconservative substitutions. The sequence of a motif conserved in all putative magnesium transporters, G-M-N, is indicated in bold. Predicted coiled-coil regions are underlined, five regions with conserved amino acid residues (CRB-1-5; conserved residue block) are shaded grey. Arrowhead: The position of the residue affected by the *dmy* mutation, after which the 15 additional residues follow in mutant MRS2.
Found at: doi:10.1371/journal.pgen.1001262.s005 (1.38 MB TIF)

Acknowledgments

The authors are grateful to M. Yokoe for excellent technical assistance.

Author Contributions

Conceived and designed the experiments: TK. Performed the experiments: TK MK ST TI YN KK. Analyzed the data: TK MK. Contributed reagents/materials/analysis tools: MA TS. Wrote the paper: TK MK JLG.

References

1. Werner H, Jung M, Klugmann M, Sereda M, Griffiths IR, et al. (1998) Mouse models of myelin diseases. Brain Pathol 8: 771–793.
2. Griffiths IR (1996) Myelin mutants: model systems for the study of normal and abnormal myelination. Bioessays 18: 789–797.
3. Meyer Zu Horste G, Nave KA (2006) Animal models of inherited neuropathies. Curr Opin Neurol 19: 464–473.
4. Kuramoto T, Sotelo C, Yokoi N, Serikawa T, Gonalons Sintes E, et al. (1996) A rat mutation producing demyelination (*dmy*) maps to chromosome 17. Mamm Genome 7: 890–894.
5. Kitada K, Guenet JL, Serikawa T (2000) Determination of the mouse homologous region for the rat *dmy* locus. J Exp Anim Sci 41: 40–43.
6. Schindl R, Weghuber J, Romanin C, Schweyen RJ (2007) Mrs2p forms a high conductance Mg^{2+} selective channel in mitochondria. Biophys J 93: 3872–3883.
7. Gregan J, Bui DM, Pillich R, Fink M, Zsurka G, et al. (2001) The mitochondrial inner membrane protein Lpe10p, a homologue of Mrs2p, is essential for magnesium homeostasis and group II intron splicing in yeast. Mol Gen Genet 264: 773–781.
8. Schock I, Gregan J, Steinhauser S, Schweyen R, Brennicke A, et al. (2000) A member of a novel Arabidopsis thaliana gene family of candidate Mg^{2+} ion transporters complements a yeast mitochondrial group II intron-splicing mutant. Plant J 24: 489–501.
9. Kuwamura M, Kanehara T, Tokuda S, Kumagai D, Yamate J, et al. (2004) Immunohistochemical and morphometrical studies on myelin breakdown in the demyelination (*dmy*) mutant rat. Brain Res 1022: 110–116.
10. Kolisek M, Zsurka G, Samaj J, Weghuber J, Schweyen RJ, et al. (2003) Mrs2p is an essential component of the major electrophoretic Mg^{2+} influx system in mitochondria. Embo J 22: 1235–1244.
11. Piskacek M, Zotova L, Zsurka G, Schweyen RJ (2009) Conditional knockdown of hMRS2 results in loss of mitochondrial Mg^{2+} uptake and cell death. J Cell Mol Med 13: 693–700.
12. Wiesenberger G, Waldherr M, Schweyen RJ (1992) The nuclear gene MRS2 is essential for the excision of group II introns from yeast mitochondrial transcripts in vivo. J Biol Chem 267: 6963–6969.
13. Devivo DC (1993) The expanding clinical spectrum of mitochondrial diseases. Brain Dev 15: 1–22.
14. Huttemann M, Zhang Z, Mullins C, Bessert D, Lee I, et al. (2009) Different proteolipid protein mutants exhibit unique metabolic defects. ASN Neuro 1.
15. Thambisetty M, Newman NJ (2004) Diagnosis and management of MELAS. Expert Rev Mol Diagn 4: 631–644.
16. Bui DM, Gregan J, Jarosch E, Ragnini A, Schweyen RJ (1999) The bacterial magnesium transporter CorA can functionally substitute for its putative homologue Mrs2p in the yeast inner mitochondrial membrane. J Biol Chem 274: 20438–20443.
17. Zsurka G, Gregan J, Schweyen RJ (2001) The human mitochondrial Mrs2 protein functionally substitutes for its yeast homologue, a candidate magnesium transporter. Genomics 72: 158–168.
18. Eshaghi S, Niegowski D, Kohl A, Martinez Molina D, Lesley SA, et al. (2006) Crystal structure of a divalent metal ion transporter CorA at 2.9 angstrom resolution. Science 313: 354–357.
19. Detmer SA, Chan DC (2007) Functions and dysfunctions of mitochondrial dynamics. Nat Rev Mol Cell Biol 8: 870–879.
20. Hung PC, Wang HS (2007) A previously undescribed leukodystrophy in Leigh syndrome associated with T9176C mutation of the mitochondrial ATPase 6 gene. Dev Med Child Neurol 49: 65–67.
21. Navarro-Sastre A, Martin-Hernandez E, Campos Y, Quintana E, Medina E, et al. (2008) Lethal hepatopathy and leukodystrophy caused by a novel mutation in MPV17 gene: description of an alternative MPV17 spliced form. Mol Genet Metab 94: 234–239.
22. Spinazzola A, Viscomi C, Fernandez-Vizarra E, Carrara F, D'Adamo P, et al. (2006) MPV17 encodes an inner mitochondrial membrane protein and is mutated in infantile hepatic mitochondrial DNA depletion. Nat Genet 38: 570–575.
23. Zafeiriou DI, Koletzko B, Mueller-Felber W, Paetzke I, Kueffer G, et al. (1995) Deficiency in complex IV (cytochrome c oxidase) of the respiratory chain, presenting as a leukodystrophy in two siblings with Leigh syndrome. Brain Dev 17: 117–121.
24. Andrews HE, Nichols PP, Bates D, Turnbull DM (2005) Mitochondrial dysfunction plays a key role in progressive axonal loss in Multiple Sclerosis. Med Hypotheses 64: 669–677.
25. Mahad DJ, Ziabreva I, Campbell G, Lax N, White K, et al. (2009) Mitochondrial changes within axons in multiple sclerosis. Brain 132: 1161–1174.
26. Lopez MF, Kristal BS, Chernokalskaya E, Lazarev A, Shestopalov AI, et al. (2000) High-throughput profiling of the mitochondrial proteome using affinity fractionation and automation. Electrophoresis 21: 3427–3440.
27. Pagliarini DJ, Calvo SE, Chang B, Sheth SA, Vafai SB, et al. (2008) A mitochondrial protein compendium elucidates complex I disease biology. Cell 134: 112–123.
28. Dheen ST, Kaur C, Ling EA (2007) Microglial activation and its implications in the brain diseases. Curr Med Chem 14: 1189–1197.
29. Merrill JE, Scolding NJ (1999) Mechanisms of damage to myelin and oligodendrocytes and their relevance to disease. Neuropathol Appl Neurobiol 25: 435–458.
30. Mitrovic B, Ignarro LJ, Montestruque S, Smoll A, Merrill JE (1994) Nitric oxide as a potential pathological mechanism in demyelination: Its differential effects on primary glial cells in vitro. Neuroscience 61: 575–585.
31. Serikawa T, Kuramoto T, Hilbert P, Mori M, Yamada J, et al. (1992) Rat gene mapping using PCR-analyzed microsatellites. Genetics 131: 701–721.
32. Kuramoto T, Kitada K, Inui T, Sasaki Y, Ito K, et al. (2001) Attractin/mahogany/zitter plays a critical role in myelination of the central nervous system. Proc Natl Acad Sci U S A 98: 559–564.
33. Zhang Y, Buchholz F, Muyrers JP, Stewart AF (1998) A new logic for DNA engineering using recombination in *Escherichia coli*. Nat Genet 20: 123–128.

Exp. Anim. 60(1), 57–63, 2011

—Original—

Kyoto Rhino Rats Derived by ENU Mutagenesis Undergo Congenital Hair Loss and Exhibit Focal Glomerulosclerosis

Takashi KURAMOTO[1)], Mitsuru KUWAMURA[2)], Fumi TAGAMI[1)], Tomoji MASHIMO[1)], Masato NOSE[3)], and Tadao SERIKAWA[1)]

[1)]Institute of Laboratory Animals, Graduate School of Medicine, Kyoto University, Sakyo-ku, Kyoto 606-8501, [2)]Laboratory of Veterinary Pathology, Osaka Prefecture University, Izumisano, Osaka 598-8531, and [3)]Department of Pathogenomics, Graduate School of Medicine, Ehime University, Toon, Ehime 791-0295, Japan

Abstract: *N*-ethyl-*N*-nitrosourea (ENU) mutagenesis is an important tool for studying gene function and establishing human disease models. Here, we report the characterization of a novel hairless mutant rat strain that carries a recessive mutation called Kyoto rhino (*krh*), which was created by ENU-mutagenesis. We produced a F344-*krh* strain through inbreeding without backcrossing to F344 rats. The *krh*/*krh* rats lost their coat hair by eight weeks of age. They also developed wrinkled skin, cystic hair canals and long curved nails by four months of age. Markedly dilated hair follicles that contained keratin debris were observed during histological analysis of the skin. The *krh* locus was mapped near the hairless (*Hr*) gene on chromosome 15. Sequence analysis revealed a nonsense mutation (c. 1238 C>A, p. S413X) in the *Hr* gene. The truncated HR protein was deduced to lack a zinc-finger domain and repression domains. In aged Hr^{krh}/Hr^{krh} rats, focal glomerulosclerosis (FGS) was observed in which collapsed glomeruli contained protein exudates in Bowman's capsule. Mesangial matrices that had proliferated in segments and foot processes that were fused in podocytes were also observed. The Hr^{krh}/Hr^{krh} rats also suffered from significant proteinuria. Given its breeding history, the F344-Hr^{krh} strain may harbor ENU-induced mutation(s) that underlie FGS in addition to having the Hr^{krh} mutation. The F344-Hr^{krh} rat is a useful model of skin disease and may provide a new model system for the examination of the pathogenesis of FGS.

Key words: disease model, hairless, mutation, nephrosis

Introduction

Hairless mutant rodents are valuable models for studying molecular mechanisms that underlie hair growth control. They are particularly valuable when searching for the genetic basis of hereditary human hair disorders.

In mice, 43 mutations are responsible for primary genetic hairlessness [7]. Among them, the most important are allelic mutations of the hairless (*Hr*) gene. The best characterized allele is the hairless (*hr*). Hr^{hr}/Hr^{hr} mice have a striking total alopecia phenotype which appears between three and four weeks of age. The pheno-

(Received 17 August 2010 / Accepted 16 September 2010)

Address corresponding: T. Kuramoto, Institute of Laboratory Animals, Graduate School of Medicine, Kyoto University, Yoshidakonoe-cho, Sakyo-ku, Kyoto 606-8501, Japan

type originates in the periorbital region and propagates in a wave-like fashion in the rostral-to-caudal direction [20]. It has been determined, through comparative studies of several distinct mouse *Hr* mutations, that the *Hr* gene product plays a key role in controlling hair follicle transformation during the catagen phase [20]. The hairless phenotype of *Hr*-mutant mice (Hr^{hr}/Hr^{hr}) is similar to that of the human disease atrichia. The disease phenotype comprises papular lesions (APL) and alopecia universalis congenital (ALUNC), complete hair loss after birth. It is a result of human *HR* mutation [2, 4, 9].

Another important mutant *Hr* of the mouse is the rhino (*rh*) mouse. Hr^{rh}/Hr^{rh} mice lose all of their hair by seven weeks of age, possess wrinkled skin and their nails overgrow. Additionally, they develop an autoimmune disease characterized by hypergammaglobulinemia, immunoglobulin deposits in the basement membrane of skin, spleen, liver, and kidney, and the presence of antinuclear antibodies which appear in young mice and increase with age [14].

Several rat hair loss mutations have been described. They are for the Charles River hairless rat [1], the Iffa Credo (IC) rat [6], the Hairless Wistar Yagi rat also known as the HWY/Slc rat [13], the Dundee experimental bald rat also known as the DEBR rat [22], the Bald rat [12], and the Hirosaki hairless rat (HHR) [17]. An intragenic deletion in the desmoglein 4 gene underlies the IC rat skin phenotype [6]. The absence of 80-kb of genomic DNA that contains five basic keratin genes is the cause of the HHR rat hairless phenotype [17].

Rat hair follicles are larger than those of mice. Therefore hairless mutant rats are attractive models for studying hair follicle development, differentiation, and cycling. Rat mutants are also good models for evaluating the effects of new drugs for treating human skin diseases. Therefore, it would be beneficial to establish new hairless rat models for these purposes.

We recently treated rats with *N*-ethyl-*N*-nitrosourea (ENU) to obtain different mutants [16]. Several hair loss phenotypes were identified by employing phenotype-driven screening. A hair loss mutant line was established by crossing mutant-type males with wild-type female littermates. Our analysis of the breeding record of this line can be used to prove that the hair loss phenotype is autosomal recessive. Thus, the mutation was named Kyoto rhino (*krh*).

In this study, we identified the *krh* mutation using a positional candidate approach and characterized the *krh/krh* rats. *krh* is a nonsense mutation of the rat *Hr* gene. *krh/krh* rats develop renal failure with massive proteinuria and focal glomerulosclerosis (FGS).

Materials and Methods

Animals

ENU-treated F344/NSlc male rats were mated with F344/NSlc female rats to generate G_1 offspring [16]. The ENU-mutagenized G_1 rats (n=42) were used as founders for the phenotype-driven screening of recessive mutations. Briefly, the G_1 rats were crossed with two F344 rats to generate G_2 offspring. The female G_2 offspring were then backcrossed with their parental G_1 rats to generate G_3 offspring. The recessive mutations induced by ENU in the G_1 rats become homozygous in the G_3 rats. Among the G_3 offspring (n=11) from a G_1 male (#E2307), three rats showed a hair loss phenotype; these rats were probands (P generation). We mated the affected rats with the normal littermates to fix the hair loss phenotype. The phenotype was fixed at the F_2 generation and the mutation was called *krh*. A mutant line was established by employing brother-sister mating (homozygous male × heterozygous female). The generation of inbreeding had reached F_6 at the end of August, 2010. The animal care and experimental procedures that were used were approved by the Animal Research Committee, Kyoto University and were carried out according to the Regulation on Animal Experimentation at Kyoto University.

Genetic mapping

Twenty N_2 rats were produced from a (BN/SsNSlc × F344-*krh/krh*)F_1 × F344-*krh/krh* backcross. The genotypes for the *krh* locus were identified on the basis of coat phenotype at four to five weeks of age. Genomic DNA was prepared from tail biopsies using an automatic DNA purification system (PI-200, Kurabo, Japan) and genotypes for *D15Rat10*, *D15Rat13*, and *D15Rat85* were determined. Linkage relationship was evaluated using the chi-square test of the Excel statistical package.

Confidence intervals ($P<0.05$) were calculated according to the method of a previous report [11].

RT-PCR and direct sequencing

Total RNA was isolated from the skin of five-week-old animals using ISOGEN (NIPPON GENE, Tokyo, Japan). RT-PCR and direct sequencing of the PCR product was carried out as described previously [15]. Rat *Hr* cDNA was amplified using the following eight primer sets: rHr-01&02 CACCTGTGGAAGGCTGCT and ACAGGGTCACTCTTGGGATG; rHr-03&04 AGGGACTACGCTGGAAGGAA and CCCAAACGTTACCGAGAGTG; rHr-05&06 GCAGGCAGCAGAATCTTTG and TCCTGTGGATGTCTCTGGTG; rHr-07&08 ACTCAAGAGGGCAGGCAGT and GGTGTTGAAGAGTCCGTGGT; rHr-09&10 CTTCCATCAACAAGGGCCTA and CTGGGCTCTCTGTGGAGTCT; rHr-11&12 GGTCAGCAGAAGGAACCAAC and TTCCAGAATGCTGTGCTGTC; rHr-13&14 GACTTAGCCTGTGGGGAATG and CTCCAAGGTTCCTGCTCCAG; rHr-15&16 GTCTCCAGGTAGCCAGACCA and GTTCCCTGCTTGTACCCAAA. The PCR products overlapped each other and spanned the entire 3,624 bp *Hr* coding sequence (CDS).

Morphological analysis

Dorsal and ventral skin samples were collected from *krh/krh* and *krh/+* littermates at two, nine and seventeen weeks of age. Mouse anti-cytokeratin (AE1/AE3, Dako Japan, Tokyo, Japan) was used for immunohistochemical analysis of the skin samples. Bound antibody was detected using horseradish peroxidase conjugated anti-mouse antibody (Histofine Simplestain MAX-PO; Nichirei, Tokyo, Japan) and 3,3'-diaminobenzidine as a chromogen (Vector Laboratories, Burlingame, CA, USA). To detect lipids, frozen sections were made from specimens that had been fixed with formalin and they were stained with Oil red O.

Organ samples of the heart, lungs, liver, pancreas, kidneys, spleen, lymph nodes, salivary glands, lacrimal glands, thyroid gland, adrenal glands, small and large intestines, and knee and foot joints, were collected from three *krh/krh* rats and three F344 rats at 40 weeks of age. They were fixed using 10% neutral buffered formalin, embedded in paraffin, cut at 4 μm in thickness, and then stained with hematoxylin and eosin (HE). To study glomerular lesions, periodic acid-Schiff (PAS) or periodic acid-methenamine-silver (PAM) staining was employed. For immunofluorescence studies, kidney samples were frozen in 22-oxacalcitriol compound (Miles Inc., Elkhart, IN, USA).

Electron microscopy

Perfusion fixation through the left ventricle was conducted with 4% paraformaldehyde in 0.1 M phosphate buffer (PB). Kidneys that had been excised were stored in 2% paraformaldehyde and 2.5% glutaraldehyde in 0.1 M PB. They were fixed with 2% osmic acid for 2 h and embedded in epoxy resin. Ultra-thin sections were double-stained with uranyl acetate and lead citrate and examined using a Hitachi H-7500 electron microscope (Hitachi, Tokyo, Japan).

Urine protein measurement

To collect urine, six male *krh/krh* rats and six F344/NSlc (+/+) rats, 40 weeks of age, were caged individually in metabolic chambers after they had been orally loaded with physiological saline at 2.5 ml/100 g body weight. Six-hour urine samples were collected and their volumes, and protein concentrations were determined. Statistical differences were determined using the Mann-Whitney U test.

Results

krh/krh rat hair loss phenotype and skin morphology

For the *krh/krh* rats, hair loss first occurred around the nose around 2 weeks after birth and extended gradually from the anterior to the posterior of the body (Fig. 1A and 1B). At around four months of age they had wrinkled skin, cystic hair canals and long curved nails.

Through histopathological analysis, markedly dilated hair follicles were observed. These cystic follicles contained a lot of keratin debris (Fig. 1C), and they stained positive for cytokeratin (Fig. 1D). The cysts were lined by a thin layer of squamous epithelium and an easily identifiable granular cell layer. The sebaceous glands that surrounded the dilated cysts were hyperplastic. Staining with Oil red O revealed that a large amount of lipids was present in the lumen of each cyst and on the

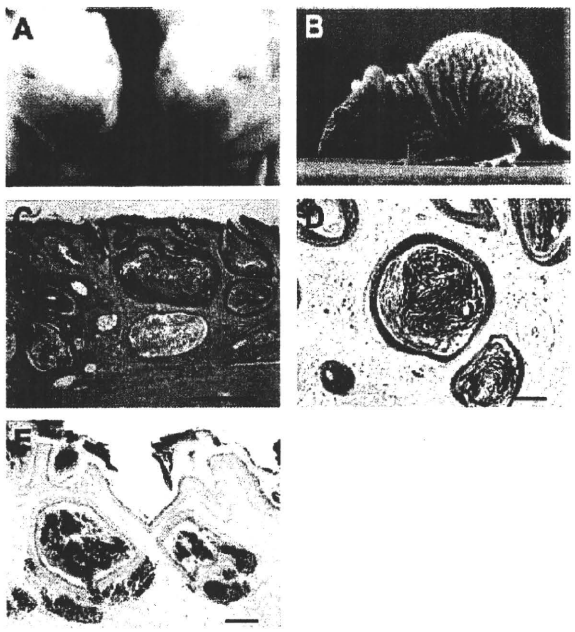

Fig. 1. Phenotypic and morphological characteristics of the Kyoto rhino rat. A: Right; a 2-week-old *krh/krh* rat with characteristic hair loss on the snout. Left; a littermate *krh/+* rat. B: Rhinocerotic appearance of a 10-week-old *krh/krh* rat. C: Histopathology of 9-week-old *krh/krh* rat skin. HE staining. Bar=500 μm. D: IHC of keratin of a 9-week-old *krh/krh* rat. Bar=100 μm. E: Oil Red O staining of a 17-week-old *krh/krh* rat. Bar=100 μm.

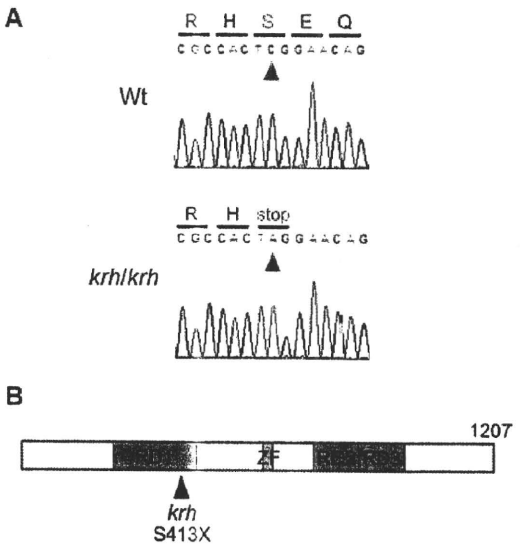

Fig. 2. Identification of the *krh* mutation. A: Results of direct sequencing of *Hr* cDNA of wild-type and *krh/krh* rats. The C-to-A nonsense mutation at position 1,238 is indicated by red arrowheads. The substitution produces a stop codon at amino acid residue 413 of protein HR. B: Schematic of the conserved domains in rat protein HR. RD1, RD2, and RD3 are used to denote the repression domains and ZF is used to denote the zinc-finger domain. The mutation site Ser413Ter is noted with a red arrowhead.

surface of the epidermis (Fig. 1E). These findings are indicators that the *krh/krh* skin and hair phenotypes are similar to those of *rh* at the *Hr* locus of the laboratory mouse [7].

krh is an Hr nonsense mutation

Hr on Chr 15 was believed to be the best candidate for *krh* and therefore the genotype of the backcross progeny was determined using genetic markers for Chr 15. We obtained 12 *krh/krh* and 8 *krh/+* rats from the (BN/SsNSlc × F344-*krh/krh*)F_1 × F344-*krh/krh* backcross. A significant linkage relationship was observed between *krh* and *D15Rat10* (42.7 Mb) with no recombination (χ^2=21.6, P<0.01), which is indicative that *krh* is located <13.9 cM away from *D15Rat10* with 95% probability [11]. *krh* was expected to span from 28.8 Mb to 56.6 Mb of Chr 15, within which the *Hr* locus (50.9 Mb) was mapped (RGSC v3.4).

Sequencing analyses of *Hr* cDNA obtained from *krh/krh* skin samples revealed that adenine (A) had been substituted for cytosine (C) at nucleotide position 1,238 from the start of the CDS (c. 1,238 C>A). This substitution resulted in a stop codon at amino acid 413 of the HR protein (p. Ser413Ter) (Fig. 2A). The truncated HR protein lacked a zinc-finger domain, a part of repression domain (RD) 1, and all of RD2 and RD3 (Fig. 2B). We characterized *krh* as an *Hr* nonsense mutation and called it Hr^{krh}.

Focal glomerulosclerosis and proteinuria in the aged Hr^{krh}/Hr^{krh} rat

Histopathological examinations of organs that were taken from Hr^{krh}/Hr^{krh} rats at 40 weeks of age were performed. No lesions that are associated with autoimmune diseases were observed, however, prominent glomerular lesions were noted in the kidneys of the Hr^{krh}/Hr^{krh} rats. These lesions were focal lesions that had collapsed glomeruli and protein exudates in Bowman capsule and the renal tubules (Fig. 3A and 3C), and segmental prolifera-

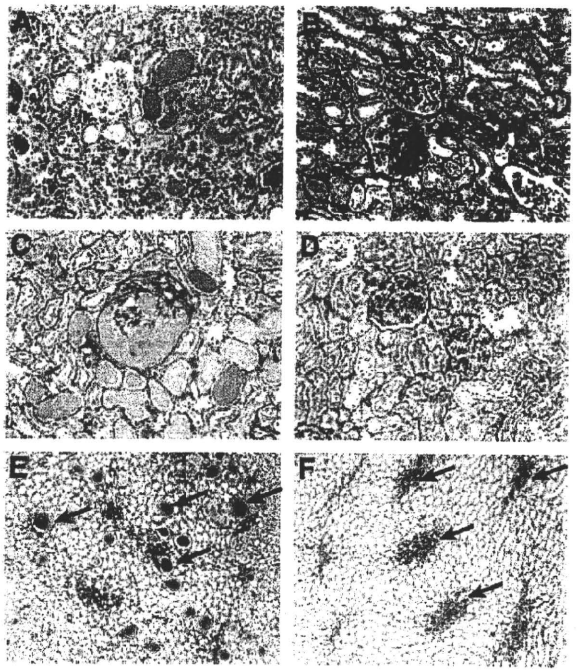

Fig. 3. Focal glomerular sclerotic lesions in 40-week-old Hr^{krh}/Hr^{krh} rat. Note that a collapsed glomerulus with protein exudates in Bowman's capsule and protein casts in renal tubules (A, C), and segmental proliferation of mesangial matrices (B, D) were seen. In the renal medulla, protein casts were notable in the collecting tubules (E) (arrows), but those in a wild-type F344 rat (+/+) were limited only to Henle's loop (F) (arrows). A: HE; B: PAM; C–F: PAS staining.

tion of the mesangial matrices (Fig. 3B and 3D). There was no inflammatory cell infiltration into the glomeruli and interstitium. In the renal medulla, protein casts were notably present in the collecting tubules (Fig. 3E). For the wild-type rats, protein casts were only observed in Henle's loop, possibly due to the effects of aging (Fig. 3F). These findings are indicators that the lesions that were observed in the F344-Hr^{krh}/Hr^{krh} rat were caused by focal glomerulosclerosis (FGS). Moreover, Hr^{krh}/Hr^{krh} rats at 40 weeks of age had proteinuria. The Hr^{krh} homozygous rats had significantly higher urine protein concentrations than age-matched wild-type rats: 152 ± 80.3 vs. 51.0 ± 38.5 mg/dl, (average ± SD), $P<0.02$ (Fig. 4).

From the electron microscopic observations, the segmental glomerular sclerotic lesions were characterized as having proliferating mesangial matrices (Fig. 5A). The proliferation was associated with the dendritic pro-

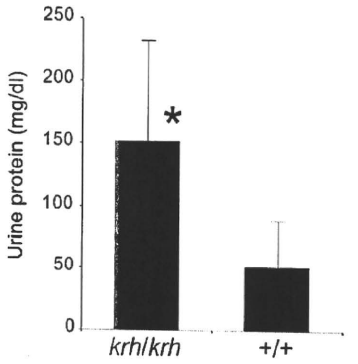

Fig. 4. Urine protein concentrations of Hr^{krh}/Hr^{krh} rats and wild-type F344 (+/+) rats. The Hr^{krh} homozygous rats had significantly higher urine protein concentrations than age-matched wild-type rats. Bars indicate standard deviation. *: $P<0.02$.

cesses of mesangial cells and on rare occasions with dense deposits in the mesangial regions. Foot process fusion was often observed in these glomeruli (Fig. 5B).

Discussion

The *krh* mutation was identified as an *Hr* nonsense mutation and therefore called Hr^{krh}. Protein HR is a nuclear receptor co-repressor for multiple nuclear receptors, such as the thyroid hormone receptor and the vitamin D receptor [23]. In the hair follicle (HF), the absence of functioning HR proteins results in the synthesis of premature and dysregulated catagen. This results in the destruction of the normal HF architecture and abrogates the HF's ability to cycle [20]. The Hr^{krh}/Hr^{krh} rat has cystic hair follicles and suffers from a premature hair cycle (Fig. 1). The truncated HR protein that is encoded by the Hr^{krh} nonsense mutation is caused by a lack of functional domains which play important roles in regulating target genes [23]. Additionally, the mutation may cause nonsense mediated mRNA decay. Therefore, it is likely that Hr^{krh} may be a loss-of-function mutation. In humans, *HR* mutations are associated with congenital alopecia, such as ALUNC and APL [2, 4, 9]. Because rats are suitably sized for handling and manipulating [5, 21], the Hr^{krh}/Hr^{krh} rat may be a useful animal model for developing therapies for these human diseases.

The aged Hr^{krh} homozygous rat has FGS which is as-

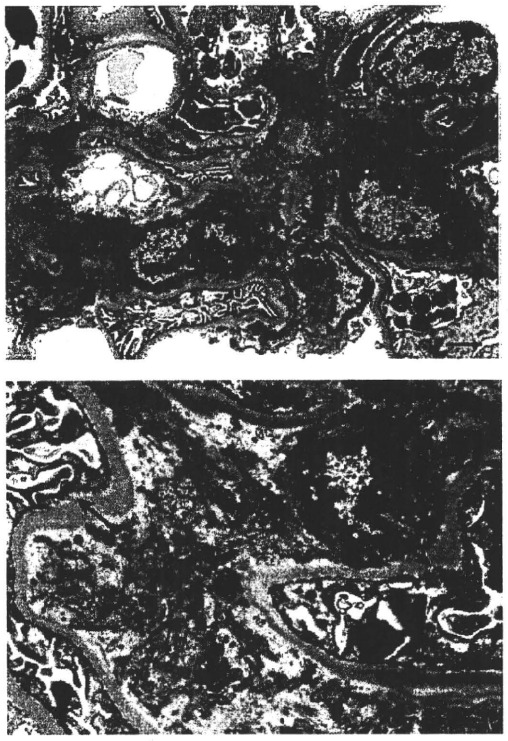

Fig. 5. Fine structures of glomerular lesions in the Hr^{krh}/Hr^{krh} rat. A: Proliferative lesions of mesangial matrices associated with significant dendritic projections from mesangial cells. Platelet aggregation was observed in a capillary loop (arrow). Intracellular hyaline droplets were significant in a podocyte (arrowhead). B: Foot process fusion (arrows) and a proliferative lesion of mesangial matrices that was not associated with dense deposits in mesangial regions and the glomerular basement membrane. Bar: 2 μm.

sociated with severe proteinuria. FGS is a descriptor for a pathological finding in the kidneys. When a nephritic range of proteinuria is observed, patients are diagnosed as having focal segmental glomerulosclerosis (FSGS). FSGS is classified by morphological variants including collapsed glomeruli, cellular proliferation, tip lesions, and diffuse mesangial proliferation [10]. The lesions that were observed in the F344-Hr^{krh} rat are characteristic of collapsed glomeruli associated with protein exudates in Bowman's capsule and may involve a collapsed variant of FSGS. Thus, the F344-Hr^{krh} rat may have potential as a model of nephritic FSGS.

FGS has not been reported for the APL or ALUNC family, and *Hr*-mutant mice, [2, 3, 7]. It is believed that FGS has a heterogeneous etiology and that it may manifest through multiple genetic factors [10]. The F344-Hr^{krh} rats were derived by employing ENU mutagenesis. The founder animals (G_1 generation) were expected to carry no more than four ENU-induced mutations in their CDS, if the CDS occupies 1% of the genome [16]. The F344-Hr^{krh} rats were mated by inbreeding without backcrossing to F344 rats to eliminate ENU-induced mutations other than the Hr^{krh} mutation. Thus, it is likely that the F344-Hr^{krh} rat may harbor mutation(s) that may play a role in the pathogenesis of FGS. FGS in Hr^{krh}/Hr^{krh} rats might be caused by unidentified mutation(s) that were induced by ENU or the combined effects of such mutation(s) with the Hr^{krh} mutation.

The Hr^{rh}/Hr^{rh} mouse has the nonsense mutation (R597X) [8] and develops hypergammaglobulinemia. The excess immunoglobulins that are produced due to this disease are deposited in the basement membranes of the skin, spleen, liver, and kidney, and antinuclear antibodies are produced. These symptoms appear in young mice and increase in severity with age [14]. Although the F344-Hr^{krh}/Hr^{krh} rat has a nonsense mutation (S413X), the mutation is not associated with an autoimmune disease or IgM, IgG, and C3 deposition in the kidneys (data not shown). Generally, pathological phenotypes that are associated with this disease are often influenced by a predisposed genetic background [18, 19]. Therefore, genes that are predisposed to causing autoimmune diseases in *rh*/*rh* mice may be absent in F344-Hr^{krh} rats. By replacing the genetic background of F344-Hr^{krh} with those of other rat strains, we might find autoimmune disease in Hr^{krh}/Hr^{krh} rats.

In summary, a novel rat mutant strain, F344-Hr^{krh}, was established that carries an *Hr* nonsense mutation (S413X). In addition to the hair loss phenotype, Hr^{krh} homozygous rats suffer from proteinuria and FGS. Therefore, F344-Hr^{krh} may have potential as a model of skin disease as well as nephritic FSGS.

Acknowledgments

This work was supported in part by Grants-in-aid for Scientific Research from the Japan Society for the Promotion of Science (21300153 to TK) and a Grant-in-aid for Cancer Research from the Ministry of Health, Labour

and Welfare. We are grateful to M. Yokoe, M. Terada, N. Takahira, and M. Sudo for their excellent technical assistance. Rat strain F344-*Hr*^{krh} (NBRP Rat No: 0471) is deposited in the National BioResource Project-Rat.

References

1. Ahearn, K., Akkouris, G., Berry, P.R., Chrissluis, R.R., Crooks, I.M., Dull, A.K., Grable, S., Jeruzal, J., Lanza, J., Lavoie, C., Maloney, R.A., Pitruzzello, M., Sharma, R., Stoklasek, T.A., Tweeddale, J., and King, T.R. 2002. The Charles River "hairless" rat mutation maps to chromosome 1: allelic with fuzzy and a likely orthologue of mouse frizzy. *J. Hered.* 93: 210–213.
2. Ahmad, W., Faiyaz ul Haque, M., Brancolini, V., Tsou, H.C., ul Haque, S., Lam, H., Aita, V.M., Owen, J., deBlaquiere, M., Frank, J., Cserhalmi-Friedman, P.B., Leask, A., McGrath, J.A., Peacocke, M., Ahmad, M., Ott, J., and Christiano, A.M. 1998. Alopecia universalis associated with a mutation in the human hairless gene. *Science* 279: 720–724.
3. Ahmad, W., Ratterree, M.S., Panteleyev, A.A., Aita, V.M., Sundberg, J.P., and Christiano, A.M. 2002. Atrichia with papular lesions resulting from mutations in the rhesus macaque (*Macaca mulatta*) hairless gene. *Lab. Anim.* 36: 61–67.
4. Ahmad, W., Zlotogorski, A., Panteleyev, A.A., Lam, H., Ahmad, M., ul Haque, M.F., Abdallah, H.M., Dragan, L., and Christiano, A.M. 1999. Genomic organization of the human hairless gene (*HR*) and identification of a mutation underlying congenital atrichia in an Arab Palestinian family. *Genomics* 56: 141–148.
5. Aitman, T.J., Critser, J.K., Cuppen, E., Dominiczak, A., Fernandez-Suarez, X.M., Flint, J., Gauguier, D., Geurts, A.M., Gould, M., Harris, P.C., Holmdahl, R., Hubner, N., Izsvak, Z., Jacob, H.J., Kuramoto, T., Kwitek, A.E., Marrone, A., Mashimo, T., Moreno, C., Mullins, J., Mullins, L., Olsson, T., Pravenec, M., Riley, L., Saar, K., Serikawa, T., Shull, J.D., Szpirer, C., Twigger, S.N., Voigt, B., and Worley, K. 2008. Progress and prospects in rat genetics: a community view. *Nat. Genet.* 40: 516–522.
6. Bazzi, H., Kljuic, A., Christiano, A.M., and Panteleyev, A.A. 2004. Intragenic deletion in the Desmoglein 4 gene underlies the skin phenotype in the Iffa Credo "hairless" rat. *Differentiation* 72: 450–464.
7. Bult, C.J., Eppig, J.T., Kadin, J.A., Richardson, J.E., and Blake, J.A. 2008. The Mouse Genome Database (MGD): mouse biology and model systems. *Nucleic Acids Res.* 36: D724–728.
8. Cachon-Gonzalez, M.B., San-Jose, I., Cano, A., Vega, J.A., Garcia, N., Freeman, T., Schimmang, T., and Stoye, J.P. 1999. The hairless gene of the mouse: relationship of phenotypic effects with expression profile and genotype. *Dev. Dyn.* 216: 113–126.
9. Cichon, S., Anker, M., Vogt, I.R., Rohleder, H., Putzstuck, M., Hillmer, A., Farooq, S.A., Al-Dhafri, K.S., Ahmad, M., Haque, S., Rietschel, M., Propping, P., Kruse, R., and Nothen, M.M. 1998. Cloning, genomic organization, alternative transcripts and mutational analysis of the gene responsible for autosomal recessive universal congenital alopecia. *Hum. Mol. Genet.* 7: 1671–1679.
10. Dagati, V. 1994. The many masks of focal segmental glomerulosclerosis. *Kid. Int.* 46: 1223–1241.
11. Friedman, J.M., Leibel, R.L., and Bahary, N. 1991. Molecular mapping of obesity genes. *Mamm. Genome* 1: 130–144.
12. Inazu, M. and Sakaguchi, T. 1984. Morphologic characteristics of the skin of bald mutant rats. *Lab. Anim. Sci.* 34: 584–587.
13. Ishii, Y., Tsutsui, S., Doi, K., and Itagaki, S. 1997. Hair follicles of young Wistar strain hairless rats: a histological study. *J. Anat.* 191: 99–106.
14. Kawaji, H., Tsukuda, R., and Nakaguchi, T. 1980. Immunopathology of rhino mouse, an autosomal recessive mutant with murine lupus-like disease. *Acta Pathol. Jpn.* 30: 515–530.
15. Kuramoto, T., Kitada, K., Inui, T., Sasaki, Y., Ito, K., Hase, T., Kawagachi, S., Ogawa, Y., Nakao, K., Barsh, G.S., Nagao, M., Ushijima, T., and Serikawa, T. 2001. Attractin/mahogany/zitter plays a critical role in myelination of the central nervous system. *Proc. Natl. Acad. Sci. U.S.A.* 98: 559–564.
16. Mashimo, T., Yanagihara, K., Tokuda, S., Voigt, B., Takizawa, A., Nakajima, R., Kato, M., Hirabayashi, M., Kuramoto, T., and Serikawa, T. 2008. An ENU-induced mutant archive for gene targeting in rats. *Nat. Genet.* 40: 514–515.
17. Nanashima, N., Akita, M., Yamada, T., Shimizu, T., Nakano, H., Fan, Y., and Tsuchida, S. 2008. The hairless phenotype of the Hirosaki hairless rat is due to the deletion of an 80-kb genomic DNA containing five basic keratin genes. *J. Biol. Chem.* 283: 16868–16875.
18. Nose, M. 2007. A proposal concept of a polygene network in systemic vasculitis: lessons from MRL mouse models. *Allergol. Int.* 56: 79–86.
19. Nose, M., Nishimura, M., and Kyogoku, M. 1989. Analysis of granulomatous arteritis in MRL/Mp autoimmune disease mice bearing lymphoproliferative genes. The use of mouse genetics to dissociate the development of arteritis and glomerulonephritis. *Am. J. Pathol.* 135: 271–280.
20. Panteleyev, A.A., Botchkareva, N.V., Sundberg, J.P., Christiano, A.M., and Paus, R. 1999. The role of the hairless (*hr*) gene in the regulation of hair follicle catagen transformation. *Am. J. Pathol.* 155: 159–171.
21. Serikawa, T., Mashimo, T., Takizawa, A., Okajima, R., Maedomari, N., Kumafuji, K., Takami, F., Neoda, Y., Otsuki, M., Nakanishi, S., Yamasaki, K., Voigt, B., and Kuramoto, T. 2009. National BioResource Project-Rat and related activities. *Exp. Anim.* 58: 333–341.
22. Sun, J., Silva, K.A., McElwee, K.J., King, L.E., and Sundberg, J.P. 2008. The C3H/HeJ mouse and DEBR rat models for alopecia areata: review of preclinical drug screening approaches and results. *Exp. Dermatol.* 17: 793–805.
23. Thompson, C.C., Sisk, J.M., and Beaudoin, G.M. 3rd. 2006. Hairless and Wnt signaling: allies in epithelial stem cell differentiation. *Cell Cycle* 5: 1913–1917.

Neurobiology of Disease 41 (2011) 261–269

Contents lists available at ScienceDirect

Neurobiology of Disease

journal homepage: www.elsevier.com/locate/ynbdi

Scn1a missense mutation causes limbic hyperexcitability and vulnerability to experimental febrile seizures

Yukihiro Ohno [a,*], Shizuka Ishihara [a], Tomoji Mashimo [b], Nobumasa Sofue [a], Saki Shimizu [a], Takuji Imaoku [a], Toshiko Tsurumi [b], Masashi Sasa [c], Tadao Serikawa [b]

[a] *Laboratory of Pharmacology, Osaka University of Pharmaceutical Sciences, Osaka 569-1094, Japan*
[b] *Institute of Laboratory Animals, Graduate School of Medicine, Kyoto University, Kyoto 606-8501, Japan*
[c] *Nagisa Clinic, Osaka 573-1183, Japan*

ARTICLE INFO

Article history:
Received 17 May 2010
Revised 15 August 2010
Accepted 19 September 2010
Available online 25 September 2010

Keywords:
Febrile seizure
$Na_v1.1$ channel
Scn1a
Missense mutation
Rat model

ABSTRACT

Mutations of the voltage-gated sodium (Na_v) channel subunit SCN1A have been implicated in the pathogenesis of human febrile seizures including generalized epilepsy with febrile seizures plus (GEFS+) and severe myoclonic epilepsy in infancy (SMEI). Hyperthermia-induced seizure-susceptible (Hiss) rats are the novel rat model carrying a missense mutation (N1417H) of Scn1a, which is located in the third pore-forming region of the $Na_v1.1$ channel. Here, we conducted behavioral and neurochemical studies to clarify the functional relevance of the Scn1a mutation *in vivo* and the mechanism underlying the vulnerability to hyperthermic seizures. Hiss rats showed markedly high susceptibility to hyperthermic seizures (mainly generalized clonic seizures) which were synchronously associated with paroxysmal epileptiform discharges. Immunohistochemical analysis of brain Fos expression revealed that hyperthermic seizures induced a widespread elevation of Fos-immunoreactivity in the cerebral cortices including the motor area, piriform, and insular cortex. In the subcortical regions, hyperthermic seizures enhanced Fos expression region–specifically in the limbic and paralimbic regions (e.g., hippocampus, amygdala, and perirhinal–entorhinal cortex) without affecting other brain regions (e.g., basal ganglia, diencephalon, and lower brainstem), suggesting a primary involvement of limbic system in the induction of hyperthermic seizures. In addition, Hiss rats showed a significantly lower threshold than the control animals in inducing epileptiform discharges in response to local stimulation of the hippocampus (hippocampal afterdischarges). Furthermore, hyperthermic seizures in Hiss rats were significantly alleviated by the antiepileptic drugs, diazepam and sodium valproate, while phenytoin or ethosuximide were ineffective. The present findings support the notion that Hiss rats are useful as a novel rat model of febrile seizures and suggest that hyperexcitability of limbic neurons associated with Scn1a missense mutation plays a crucial role in the pathogenesis of febrile seizures.

© 2010 Elsevier Inc. All rights reserved.

Introduction

Febrile seizures (FS) are the most common type of seizures in childhood, often occurring between 6 months and 5 years of age. Although most FS are generally benign, one-third are complex and exhibit persistent and/or recurrent seizures (Fetveit, 2008; Scantlebury and Heida, 2010; Shinnar, 2003). Specifically, patients of generalized epilepsy with febrile seizures plus (GEFS+) exhibit FS in childhood progressing to generalized epilepsy in adults and, in some cases, accompany variable symptoms including tonic–clonic, absence, and/or myoclonic seizures (Scheffer and Berkovic, 1997). Severe myoclonic epilepsy in infancy (SMEI) is more severe usually beginning within the first 6 months after birth, followed by progressive worsening of seizures associated with ataxia and mental decline (Dravet et al., 2005; Incorpora, 2009). Although familial or twin studies have shown that genetic predisposition contributes to the etiology of FS (Baulac et al., 2004; Baulac and Baulac, 2009; Nakayama, 2009), the causative genes and pathogenic mechanisms underlying human FS are still elusive.

Voltage-gated sodium (Na_v) channels mediate the generation and propagation of action potentials in electrically excitable cells such as neurons and muscles. They are classified into 9 subtypes encompassing $Na_v1.1$ to $Na_v1.9$ and have a common structure composed of 4 homologous domains, each of which contains voltage-sensor and pore-forming regions. Among these subtypes, $Na_v1.1$ channels have been implicated in the pathogenesis of multiple types of FS (Meisler and Kearney, 2005; Ragsdale, 2008). Specifically, more than 200 mutations in human $Na_v1.1$ channel α subunit SCN1A have been reported in patients with FS

Abbreviations: ACF, artificial cerebrospinal fluid; FS, febrile seizure; GEFS+, generalized epilepsy with febrile seizures plus; Na_v, voltage-gated sodium; PBS, phosphate-buffered saline; IR, immunoreactivity; SMEI, severe myoclonic epilepsy in infancy.

* Corresponding author. Fax: +81 72 690 1053.
E-mail address: yohno@gly.oups.ac.jp (Y. Ohno).

Available online on ScienceDirect (www.sciencedirect.com).

0969-9961/$ – see front matter © 2010 Elsevier Inc. All rights reserved.
doi:10.1016/j.nbd.2010.09.013

including GEFS+ and SMEI (Meisler and Kearney, 2005; Ragsdale, 2008). The 13 SCN1A mutations found in patients with GEFS+ are known to be missense mutations, while about half of the SMEI mutations are missense and the remaining are truncated mutations (e.g., nonsense or frame-shift mutations) (Meisler and Kearney, 2005; Mulley et al., 2005). In addition, recent studies have shown that haploinsufficiency of $Na_v1.1$ channel causes hypersusceptibility to hyperthermic seizures and sporadic spontaneous seizure in mice, which accompanied a marked reduction in sodium currents in inhibitory GABAergic neurons (Yu et al., 2006; Oakley et al., 2009; Martin et al., 2010). All these findings indicate a close relationship between the $Na_v1.1$ channel function and the etiology of FS. Nonetheless, due to the diversity of functional changes of $Na_v1.1$ channels in patients with FS (Meisler and Kearney, 2005; Catterall et al., 2010), the precise mechanism and functional relevance of the SCN1A mutations underlying the pathogenesis of FS remain to be clarified.

Using the gene-driven *N*-ethyl-*N*-nitrosourea mutagenesis, we have recently generated a rat model which carries a missense mutation (N1417H) in the third pore-forming region of Scn1a (Mashimo et al., 2010). We designated them hyperthermia-induced seizure-susceptible (Hiss) rats because of their high susceptibility to hyperthermia-induced seizures. Since missense mutations in the pore-forming region of $Na_v1.1$ channels are frequently reported in patients with SMEI or GEFS+ (Meisler and Kearney, 2005; also see Fig. 1), Hiss rats may serve as a useful FS model with a genetic background similar to that of SMEI or GEFS+. Indeed, the mutation site in Hiss rats is very close to one (V1428A) of the GEFS+ mutations (Sugawara et al., 2001). In our previous studies (Mashimo et al., 2010), Hiss rats at a very young age (1–5 weeks old) exhibited a high susceptibility to hyperthermia-induced seizures. Electrophysiological analysis of the N1417H mutant channels or hippocampal neurons dissociated from Hiss rats revealed that N1417H mutation causes a hyperpolarized shift in the voltage dependency of $Na_v1.1$ channel inactivation and a slight increase in persistent leak current. In addition, hippocampal bipolar neurons (i.e., GABAergic interneurons) exhibited a significant decrease in spike amplitude, indicating reduced function of $Na_v1.1$ channels. These changes in $Na_v1.1$ functions were specifically observed in the biplolar neurons but not in the pyramidal neurons (Mashimo et al., 2010). Thus, our findings suggest that the Scn1a missense mutation impairs functions of the hippocampal GABAergic neurons to confer FS susceptibility. Nonetheless, the functional relevance of the Scn1a missense mutation *in vivo* and its mechanism underlying the vulnerability of animals to hyperthermic seizures remain to be determined.

In the present study, therefore, we further conducted behavioral and neurochemical studies to clarify pathophysiological mechanisms underlying the seizure vulnerability in Hiss rats. In addition, responses of hyperthermic seizures in Hiss rats to antiepileptic drugs were also evaluated to assess their clinical relevance as a human FS model. The present results show that the N1417H mutation of Scn1a markedly enhances the excitability of the corticolimbic neural circuit and the limbic vulnerability to hyperthermic seizures. Hiss rats seem to be a useful rat model for understanding the etiology of FS and also for searching new drugs to treat FS.

Materials and methods

Animals

Hiss rats (F344-*Scn1a*$^{Kyo811/Kyo811}$) were obtained from the National BioResource Project for the Rat (NBRPR#0455) in Japan. As reported previously (Mashimo et al., 2010), Hiss rats carry homozygous

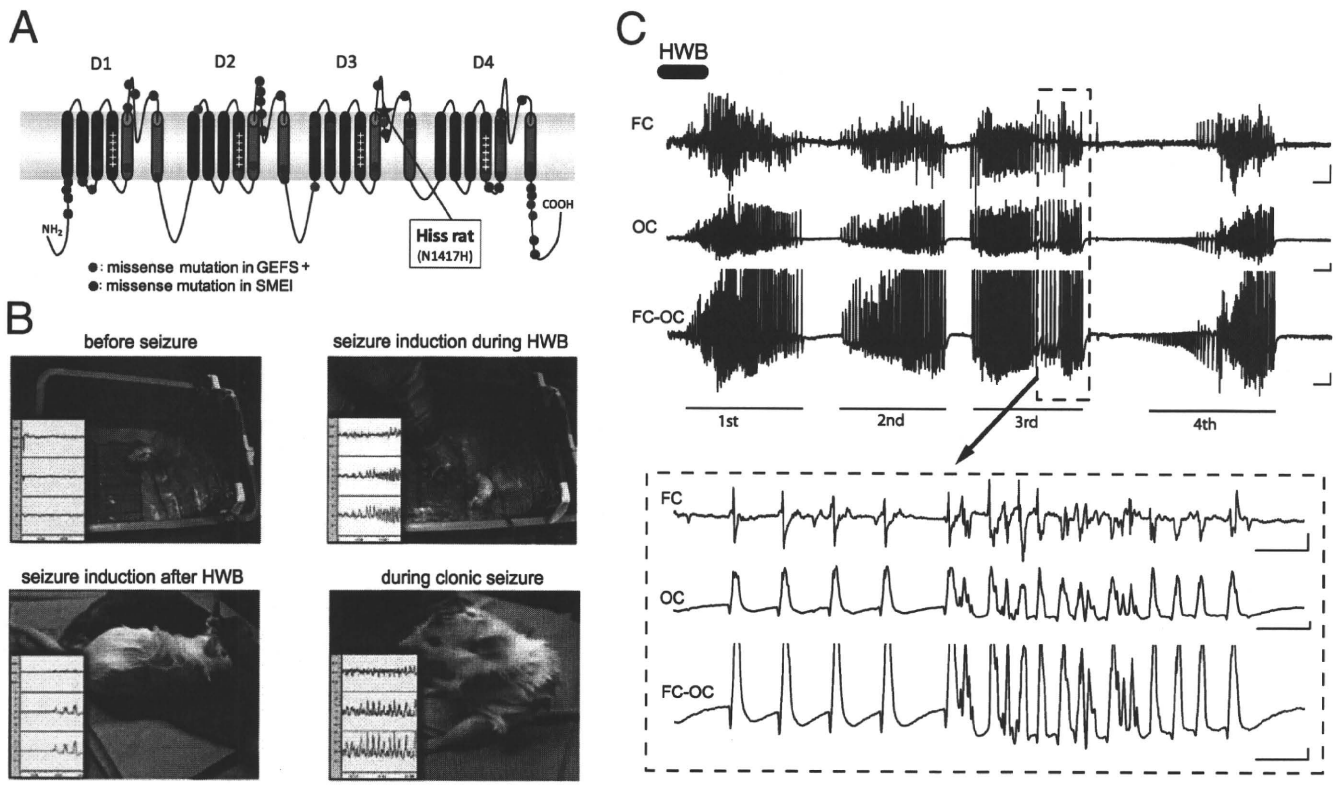

Fig. 1. Hyperthermic seizures and EEG in Hiss rats. (A) Structure of Scn1a and location of the missense mutation N1417H in Hiss rats. Scn1a consists of 4 homologous domains (D1–D4), each of which contains voltage-sensor and pore-forming regions. As a reference, missense mutation sites reported in GEFS+ and SMEI are also shown (Meisler and Kearney, 2005). (B) Photos illustrating induction of hyperthermic seizures and simultaneously monitored EEG in Hiss rats. Hiss rats were immerged in a hot water bath (HWB: 45 °C) for a maximum of 5 min or until a seizure occurred. Cortical EEG was simultaneously monitored under freely-moving conditions. All Hiss rats mainly developed clonic seizures (barely tonic–clonic seizures), which usually repeated even after HWB. (C) Typical paroxysmal discharges in Hiss rats. Solid lines (1st–4th) under EEG chart indicate the period of clonic seizures. Calibration: upper panel, 100 μV and 2 sec; lower panel, 100 μV and 1 sec.

Scn1a$^{Kyo81/Kyo8111}$ alleles, where *Scn1a* gene has a missense mutation N1417H in the third pore-forming region of $Na_v1.1$ channels (Fig. 1). Hiss rats were backcrossed more than 5 generations against F344/NSlc inbred background to eliminate mutations in chromosomal regions other than the *Scn1a* locus. F344/NSlc (F344) rats were used as control animals. The animals were kept and bred at the Institute of Laboratory of Animals, Graduate School of Medicine, Kyoto University in air-conditioned rooms (24±2 °C and 50%±10% relative humidity) under a 14-h light/10-h dark cycle (lights on: 7:00 a.m.). The housing conditions and the animal care methods complied with the Guidelines for Animal Experiments of Kyoto University. The experimental protocols of this study were also approved by the Experimental Animal Research Committee at Osaka University of Pharmaceutical Sciences.

Hyperthermic seizure induction and EEG recording

Male juvenile Hiss or F344 rats (4 weeks old) were used. To implant EEG recording electrodes, animals were anesthetized with pentobarbital (40 mg/kg, i.p.) and fixed in a stereotaxic instrument (David Kopf Instruments, CA, USA). Small holes were made in the skull, and silver ball electrodes were placed on the surface of the right or left frontal and occipital cortex. A reference electrode was placed on the frontal cranium. The electrodes were then connected to a miniature plug and fixed to the skull with dental cement. After a 1-week recovery period, animals with chronically implanted electrodes were subjected to the following experiments.

Hyperthermic seizures were evoked by immersing the animals in a hot water bath as published previously (Mashimo et al., 2010). Briefly, the animals were placed in a temperature-controlled water bath (30 cm×60 cm×60 cm) containing about 15 cm depth 45 °C water for a maximum of 5 min or until a seizure occurred. Under freely moving conditions, cortical EEG was recorded simultaneously with behavioral observation using an amplifier (MEG-6108; Nihon Kohden) and a thermal alley recorder (RTA-1100; Nihon Kohden, Tokyo, Japan). The recorded signals were stored in a computer (PowerLab ML845; AD Instruments Japan, Nagoya, Japan) for later analysis.

Forebrain Fos expression following hyperthermic seizures

Male juvenile Hiss or F344 rats (4 weeks old) were subjected to the hyperthermic seizure experiments in the same manner as described previously. Two hours after the hyperthermic seizure or the end (5 min) of bathing, the animals were deeply anesthetized with pentobarbital (80 mg/kg, i.p.), transcardially perfused with ice-cold phosphate-buffered saline (PBS) and then with 4% formaldehyde solution. The brains were removed from the skull and placed in fresh fixative for at least 24 hours. After postfixation, coronal sections (30 μm thickness) were cut from each brain using a Microslicer (DSK-3000, Dosaka, Kyoto Japan).

The staining of Fos-immunoreactivity (IR) was performed by a method published previously (Ohno et al., 2009). Briefly, slices were washed with PBS containing 0.3% Triton X-100, and incubated for 2 hours in the presence of 2% normal rabbit serum, and then again in the presence of 2% normal rabbit serum and goat c-Fos antiserum (Santa Cruz Biotechnology Inc., Santa Cruz, CA) for an additional 18–36 hours. After washing with PBS, the sections were incubated with a biotinylated rabbit anti-goat IgG secondary antibody (Vector Laboratories, Burlingame, CA) for 2 hours. The sections were then incubated with PBS containing 0.3% hydrogen peroxide for 30 min to inactivate the endogenous peroxidase. Thereafter, the sections were washed with PBS and incubated for 2 hours with avidin–biotinylated horseradish peroxidase complex (Vectastain ABC Kit). Fos-IR was visualized by the diaminobenzidine–nickel staining method.

Fos expression was quantified by counting the number of Fos-IR-positive nuclei in the following regions (Paxinos and Watson, 2007): 1) the cerebral cortices = the medial prefrontal cortex (mPFC), motor cortex (MC), sensory cortex (SC), agranular insular cortex (AIC), piriform cortex (Pir), auditory cortex (AuC); 2) the limbic/paralimbic areas = CA1, CA3, and dentate gyrus (DG) of the hippocampus, basomedial amygdaloid nucleus (BMA), perirhinal–entorhinal cortex (PRh–Ent), cingulated cortex (CgC), lateral septal nucleus (LS), core (AcC), and shell (AcS) parts of the nucleus accumbens; 3) the basal ganglia = dorsolateral (dlST) and dorsomedial (dmST) striatum and globus pallidus (GP); 4) the diencephalon = paratenial (PT), anteromedial (AM), centromedial (CM) and ventromedial (VM) thalamus, lateral habenula (LHb), anterior (AH), posterior (PH), and dorsomedial (DMH) hypothalamus; 5) the lower brainstem = locus coeruleus (LC), central gray (CG), pontine reticular nucleus (PnR), gigantocellular reticular nucleus (GiR), and inferior olivary nucleus (IO). The number of Fos-IR-positive nuclei was counted within a 350×350 μm^2 grid laid over each of the above brain regions by observers who were blinded regarding the seizure incidence.

Hippocampal afterdischarges

Male Hiss or F344 rats (8–10 weeks old) were used. Under pentobarbital (40 mg/kg, i.p.) anesthesia, animals were chronically implanted with electrodes as described previously. Namely, a silver ball electrode was placed on the surface of the right frontal cortex and a stainless-steel bipolar electrode was inserted to the ipsilateral hippocampus (P: 3.8, L: 2.0, H: −2.2 mm from the cortical surface) for EEG recording. A bipolar stimulation electrode was also inserted to a position 0.5 mm anterior to the recording site for local stimulation of the hippocampus. All electrodes including a reference electrode were then connected to a miniature plug and fixed to the skull.

After a 1-week recovery period, animals were subjected to the assessment of the stimulus threshold for hippocampal afterdischarges. Briefly, hippocampal and cortical EEG were recorded under freely moving conditions. Local stimulation consisting of square pulses (duration: 100 μsec, frequency: 20 Hz) was then applied to the hippocampus for 5 sec with increasing intensity by 25 μA a step, and the stimulus threshold for induction of the hippocampal afterdischarges was measured.

Evaluation of the effects of antiepileptic drugs

Juvenile Hiss rats of either sex (4 weeks old) were used. Animals were given either antiepileptic drug as follows; diazepam (0.5 and 1 mg/kg, i.p.), sodium valproate (100–300 mg/kg, i.p.), ethosuximide (100 mg/kg, i.p.) and phenytoin (20 and 40 mg/kg, i.p.). Thirty minutes after the drug treatment, animals were subjected to the hyperthermic seizure experiments as described previously. The number of seizure incidences, total duration of seizures (i.e., sum of the duration of each seizure), and latency for the first seizure induction were compared with those of the control values with the vehicle alone. In a separate series of experiments, the effects of antiepileptics on the body (rectal) temperature of Hiss rats were also examined. For these studies, animals were given the above doses of the antiepileptic drugs and, 30 min later, the rectal temperature was measured.

Drugs

The drugs used in this study were as follows: sodium valproate, ethosuximide and phenytoin (Sigma-Aldrich), and diazepam (Cercine®, Takeda Pharmaceuticals Co., Ltd., Osaka, Japan). Diazepam, sodium valproate, and ethosuximide were dissolved and/or diluted with physiological saline. Phenytoin was first dissolved in a small amount of 0.5 N NaOH and then diluted with saline. The

Vectastain ABC kit and DAB substrate were purchased from Vector Laboratories (CA, USA). All other reagents were obtained from commercial sources.

Statistical analysis

Data are expressed as the mean ± SEM. The statistical significance of differences in the number of Fos-IR-positive cells, the threshold level of hippocampal afterdischarges, the number and latency of spike generation in the hippocampal CA1 neurons, and the effects of antiepileptic drugs between two groups (Hiss and F344 rats) was determined by the Student's *t*-test. Comparisons of the parameters among multiple groups were analyzed by one-way ANOVA and Tukey's *post-hoc* multiple comparison test.

Results

Hyperthermic seizures in Hiss rats

We have previously demonstrated that Hiss rats show much higher susceptibility than F344 rats to seizures induced by stimulation of hot water (45 °C) bathing, with a significantly lower body (rectal) temperature (Mashimo et al., 2010). In this study, we measured EEG epileptiform discharges during hyperthermic seizures and quantified the latency for seizure induction, number of seizures, duration of each seizure and total duration of all seizures. Juvenile Hiss or F344 rats, which were chronically implanted with EEG electrodes, were placed in a 45 °C hot water bath for 5 min (Fig. 1). Under these conditions, none of F344 rats exhibited any seizures or abnormal behaviors during 5 min of bathing. However, all Hiss rats ($N=5$) examined

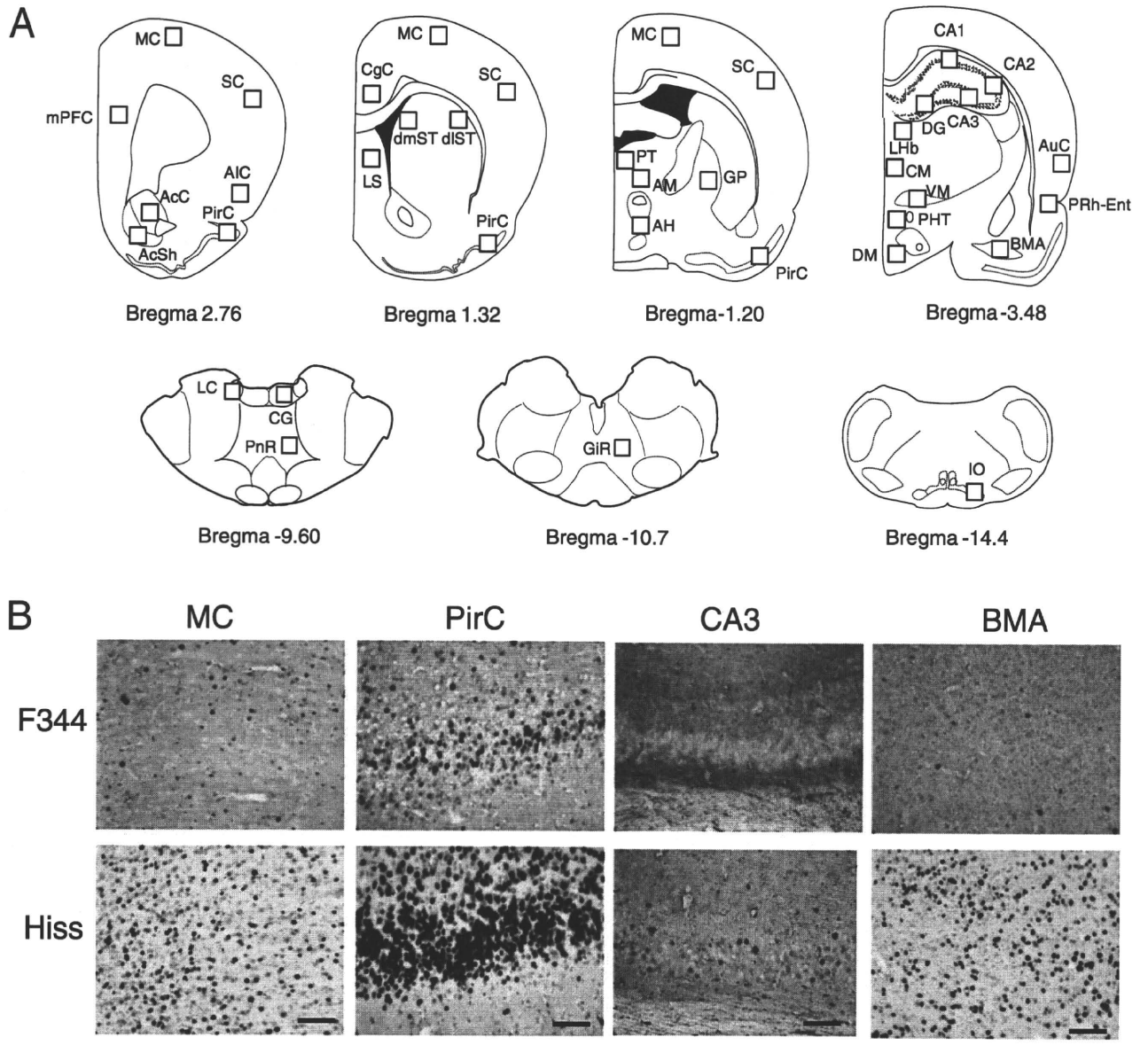

Fig. 2. Fos expression analysis following hyperthermic seizures. (A) Schematic illustrations of the brain sections selected for quantitative analysis of Fos-IR-positive cells. An anteroposterior coordinate (distance from the bregma) is shown on the bottom of each brain section. Open squares in each section indicate the sample areas analyzed; mPFC: the medial prefrontal cortex, MC: motor cortex, SC: sensory cortex, AIC: agranular insular cortex, PirC: piriform cortex, AcC and AcS: core and shell regions of the nucleus accumbens, respectively, CgC: cingulated cortex, LS: lateral septum, dlST and dmST: dorsolateral and dorsomedial striatum, respectively, GP: globus pallidus, PT, AM, CM, and VM: paratenial, anteromedial, centromedial, and ventromedial thalamus, respectively, LHb: lateral habenula, AH, PH, and DMH: anterior, posterior and dorsomedial hypothalamus, respectively, PRh–Ent: perirhinal–entorhinal cortex, AuC: auditory cortex, DG: dentate gyrus of the hippocampus, BMA: basomedial amygdaloid nucleus, LC: locus coeruleus, CG: central gray, PnR: pontine reticular nucleus, GiR: gigantocellular reticular nucleus, IO: inferior olivary nucleus. (B) Representative photographs illustrating the Fos-IR-positive cells in the MC, PirC, CA3 of the hippocampus and BMA in Hiss and F344 rats. Scale bar: 100 μm.